Connecting near-field and far-field earthquake triggering to dynamic strain

Nicholas J. van der Elst[1] and Emily E. Brodsky[1]

[1] Any earthquake can trigger more earthquakes. This triggering occurs in both the classical aftershock zone as well as the far field. These populations of triggered earthquakes may or may not be distinct in terms of triggering mechanism. Here we look for a distinction between the populations by examining how the observed intensity of triggering scales with the amplitude of the triggering strain in each. To do so, we apply a new statistical metric based on earthquake interevent times to a large data set and measure earthquake triggering as a function of dynamic strain amplitude, where strain is estimated from empirical ground motion regressions. This method allows us to identify triggering at dynamic strain amplitudes down to 3×10^{-9}, orders of magnitude smaller than previously reported. This threshold appears to be an observational limit and shows that extremely small dynamic strains can trigger faults that are sufficiently near failure. Using a probabilistic model to transform measured interevent times to seismicity rate changes, we find that triggering rates in the far field scale with peak dynamic strain. This scaling, projected into the near field, accounts for 15%–60% of earthquakes within 6 km of magnitude 3–5.5 earthquakes. Statistical seismicity simulations validate the interevent time method and show that the data are consistent with the number of far-field triggered earthquakes being linearly proportional to peak dynamic strain. We interpret the additional near-field component as reflecting either static stress triggering, more effective dynamic triggering at higher frequencies, or a concentration of aftershock nucleation sites very near main shocks.

1. Introduction

[2] Triggered earthquakes provide a window into the physics of earthquake nucleation because the forces initiating rupture can be inferred. Because the strain at which a fault is triggered is a measure of its strength, it may be possible to gain insight into the distribution of fault strength by studying the statistics of earthquake triggering [*Brodsky and Prejean*, 2005; *Gomberg*, 2001].

[3] One strategy for ultimately determining the processes involved in triggering is to first identify the stresses that activate the process. The types of stresses that have been proposed as the agents by which one fault transmits a triggering signal to another include coseismic static strain changes, progressive postseismic strain changes (including afterslip and viscous creep), and dynamic strains from radiated seismic waves [*Freed*, 2005]. These agents may each trigger earthquakes through a number of mechanisms, including direct Coulomb frictional failure, reduction in fault strength, and pore fluid pressure changes. Different triggering agents may be expected to be relatively more or less effective at activating different failure mechanisms. Therefore, understanding the relative contribution of triggering agents may help constrain triggering mechanisms.

[4] The proposed triggering agents have different strengths and weaknesses in explaining observed triggering. Coseismic static strain changes are the increase or decrease in strain at one fault due to the relaxation of strain at another during an earthquake. Static strain changes are permanent and therefore can easily explain triggering for an extended period of time [*King et al.*, 1994], but the stresses decay in amplitude quickly with distance away from a fault and are thus unlikely to trigger distant earthquakes. Multiple stress interactions, i.e., secondary triggering or aftershocks of aftershocks, can extend the reach of static stresses to a few times the length of the primary rupture [*Ziv*, 2003], but not to the tens of times observed for remote triggering [*Hill et al.*, 1993]. Postseismic static strain changes are generated by afterslip or lower crustal ductile creep and also produce prolonged stresses. Afterslip produces a quasi-static near-field stress change that has comparable distance decay to coseismic static stress changes and thus cannot explain triggering at great distances. Viscous deformation can propagate to great dis-

[1]Department of Earth and Planetary Science, University of California, Santa Cruz, California, USA.

tances but takes years to reach hundreds of kilometers [*Freed and Lin*, 1998; *Pollitz et al.*, 1998] and thus cannot explain distant triggering that is sometimes seen within days or even seconds [*West et al.*, 2005]. Dynamic triggering is associated with transient strains carried by radiated seismic waves [*Hill and Prejean*, 2007]. Dynamic strains decay less quickly with distance and therefore do well at explaining remote triggering but present a challenge in explaining prolonged triggering [*Brodsky*, 2006; *Gomberg*, 2001].

[5] The above summary highlights that there is more certainty about the agent of triggering for a special subset of earthquake triggering: distant triggering over time scales of less than a few years. These remotely triggered earthquakes are believed to result entirely from dynamic triggering, both because static strains are negligible at large distances, and because distant triggering often coincides with the arrival of surface waves [*Anderson et al.*, 1994; *Brodsky et al.*, 2000; *Gomberg and Johnson*, 2005; *Hill et al.*, 1993]. On the other hand, short-range triggering is much more ambiguous and has been attributed to static, postseismic, or dynamic agents by different researchers [*Felzer and Brodsky*, 2006; *Gomberg et al.*, 2003; *Kilb et al.*, 2000; *Perfettini and Avouac*, 2007; *Pollitz and Johnston*, 2006; *Stein et al.*, 1994; *Velasco et al.*, 2008]. Spatial correlations between calculated coseismic static stress fields and aftershock patterns appear to support coseismic static stress triggering [*King et al.*, 1994; *Stein et al.*, 1994]. On the other hand, correlations between temporal aftershock evolution and geodetic strain measurements support progressive postseismic strain [*Freed and Lin*, 1998; *Peng and Zhao*, 2009; *Perfettini and Avouac*, 2007]. Still other studies that compare near-field aftershock locations to the static and dynamic strains for earthquakes with strong directivity conclude that dynamic strains correlate better with the ensuing seismicity [*Gomberg et al.*, 2003; *Kilb et al.*, 2000].

[6] In this study, we exploit the understanding that dynamic strain is the dominant triggering agent at large distances and relatively short time scales in order to constrain the contribution of additional triggering agents in the near field. We first determine an empirical relationship between a measure of triggering intensity and peak dynamic strain in the far field based on the waiting time to early triggered earthquakes. Then we compare this far-field relationship to near-field observations to assess the proportion of near-field earthquakes that can be explained by the far-field proportionality. We ultimately find that dynamic triggering can account for a significant portion of near-field aftershocks, but that there is an additional triggering component in the near field. Whether this reflects additional triggering agents (e.g., static strain, afterslip) or the effect of second-order aspects of the dynamic strain (e.g., duration, frequency) we cannot resolve. In the process, we develop a measure of earthquake triggering that is significantly more sensitive to low triggering rates than previous measures and place a new bound on the threshold for far-field dynamic triggering.

[7] The first several sections of this article concern the development of the triggering metric. First, we define a statistic based on earthquake interevent times and establish the expectation for this statistic, assuming a simple probabilistic model for earthquake occurrence times. Next, we delineate populations on the basis of local dynamic strain and describe the data selection and processing. In section 4,

we apply the method and show that the dynamic triggering relationship determined for far-field quakes can account for roughly half of near-field aftershock triggering. We also report a new estimate on the dynamic triggering threshold in California of 3×10^{-9} strain, several orders of magnitude lower than previous estimates. A statistical seismicity simulation is then used to interpret and validate the results. Finally, we evaluate the implications and robustness of the results.

2. Measuring Earthquake Rate Changes Using Interevent Times

[8] A comparison of triggering rates in the near field and far field requires a metric that can be applied to both populations of earthquakes. This metric needs to be sensitive enough to detect the very small triggering rates associated with the very small dynamic strains common to the far field. Previously, triggered earthquakes have been identified by inspecting seismicity rates [*Harrington and Brodsky*, 2006; *Hill et al.*, 1993; *Stark and Davis*, 1996] or by filtering waveforms to emphasize short-period energy within the surface wave trains of large, distant earthquakes [*Brodsky et al.*, 2000; *Hill and Prejean*, 2007; *Velasco et al.*, 2008]. Quantitative estimates of triggering usually involve calculating the likelihood of observing a number of posttrigger events given the previous seismicity rate [*Anderson et al.*, 1994; *Gomberg et al.*, 2001; *Hough*, 2005]. If the likelihood of the rate increase occurring by chance is low enough, triggering is inferred.

[9] Any estimate that computes the likelihood of triggering based on counting the number of triggered earthquakes relative to a pretrigger count, like the β statistic [*Matthews and Reasenberg*, 1988], is limited in several ways. First, the pretrigger seismicity rate must be resolved for comparison, and this is inherently difficult. Because most earthquakes occur as clusters of aftershocks, the seismicity rate is always changing. Background seismicity level should therefore be measured at a time as close to the purported trigger as possible in as short a window as possible. Different areas will permit different length windows depending on their background level of seismicity, and thus, a constant window for an entire data set may not sufficiently capture the data. Second, an earthquake count can only resolve an integer increase in the number of earthquakes for any individual sequence. A slight advancement in the timing of subsequent earthquakes will only rarely result in an additional triggered earthquake within the counting time window, so only large levels of triggering can be resolved with statistical significance. Finally, an earthquake count also includes all secondarily triggered earthquakes, that is, aftershocks of aftershocks. These secondary earthquakes are not strictly problematic, because they should still be produced in proportion to the number of primary triggered earthquakes when averaged over many events, but they complicate the relationship between trigger amplitude and number of triggered quakes by introducing variance into the measurements.

[10] To detect triggering at very low dynamic strain amplitudes, our metric must use an adaptive time window to measure background rates, be sensitive to small increases in seismicity rates, and be insensitive to secondary aftershocks.
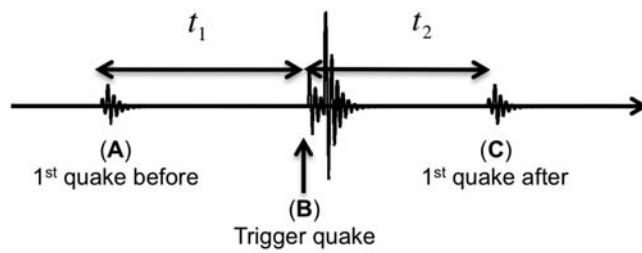
Figure 1. Cartoon timeline illustrating the variables contributing to the interevent time ratio R (equation (1)). The trigger earthquake is labeled B, and the first earthquake before and after the trigger are labeled A and C, respectively. The time t_1 is the time to the first earthquake before the trigger, and t_2 is the waiting time to the first earthquake after the trigger.

2.1. Interevent Time Ratio R

[11] We meet the above requirements by developing a statistic based only on the interevent times between the last earthquake before a trigger and the first earthquake after. We define the interevent time ratio R as

$$R \equiv \frac{t_2}{t_1 + t_2}, \qquad (1)$$

where t_1 and t_2 are the waiting times to the first earthquake before and after the putative trigger (Figure 1). The interevent time ratio R was originally developed to study triggered quiescence [*Felzer and Brodsky*, 2005]; we use it here to look for a triggered rate increase.

[12] Because R is normalized by the average seismicity rate at the time of the trigger, we can pool and compare measurements made within a highly heterogeneous earthquake catalog. The strategy in this study is to measure the distribution of R on a population of earthquakes that are subject to similar triggering conditions. For instance, the population can be drawn from a variety of areas subject to the same dynamic strain. The metric R is a random variable distributed between 0 and 1. If there is no triggering in the population and t_2 is on average equal to t_1, then R is distributed uniformly with a mean value $\overline{R} = \frac{1}{2}$. On the other hand, if triggering does occur, t_2 will be on average smaller than t_1 and $\overline{R} < \frac{1}{2}$. More triggering results in a smaller $\overline{R}$ (Figure 2). Therefore, the statistic $\overline{R}$ provides a measure of triggering intensity within a population of earthquakes.

[13] The interevent time ratio R naturally solves the three problems identified with earthquake counting methods by defining an appropriate time window for each event based on the interevent times, utilizing the statistics of large populations, and focusing on the first recorded earthquake rather than the entire triggered sequence.

[14] One of the unusual features of the interevent time method is that there is no time limit for the inclusion of triggered events. Both instantaneous and delayed triggering are included in the measurements. This comprehensiveness is desirable because of issues of catalog completeness, as well as the physical implications of delayed triggering. Instantaneous triggering ($t_2 \sim 0$) should be reflected in the R distribution as a strong spike at $R \sim 0$ with a uniformly depressed probability density at higher values. Delayed

triggering ($0 < t_2 < t_1$) should cause the spike to be spread out to larger R values (e.g., Figure 2). In principle, the distribution of R should therefore reflect the time decay of the triggered rate change. For the purposes of this study, however, we restrict ourselves to calculations involving the sample mean $\overline{R}$ and do not consider the precise shape of the distribution. We will return to the issue of delayed triggering at the end of the paper after the metric has been implemented.

2.2. Interpreting R as Seismicity Rate Change

[15] The purpose of this study is to compare dynamic triggering levels in far-field and near-field populations of triggers. However, the range of dynamic strain amplitudes observable in each population is different, at least in the California study region focused on here. This is because even the largest far-field earthquakes generate only low-amplitude waves at great distance (so small that equivalent near-field triggers are too low in magnitude to be detected in regional catalogs). Consequently, we measure the scaling of $\overline{R}$ with dynamic strain in each population and compare the respective trends. Because $\overline{R}$ must asymptote to 0.5 for zero rate change and to 0 for extreme rate increases, $\overline{R}$ must scale nonlinearly with rate change. This nonlinearity complicates the comparison of trends between the two dynamic strain ranges. In order to compare triggered rate changes in the two populations, we first establish the expected behavior of $\overline{R}$ as a function of rate change.

[16] To derive the expectation of R as a function of seismicity rate change, we use a model that relates interevent times to earthquake rate. If earthquake occurrence were perfectly periodic and uniform, the expectation of R would follow directly from equation (1) with t_1 and t_2 equal to the inverse of the earthquake rate. However, earthquakes are for the most part not periodic. Detailed studies of earthquake catalogs find that the distribution of interevent times is best
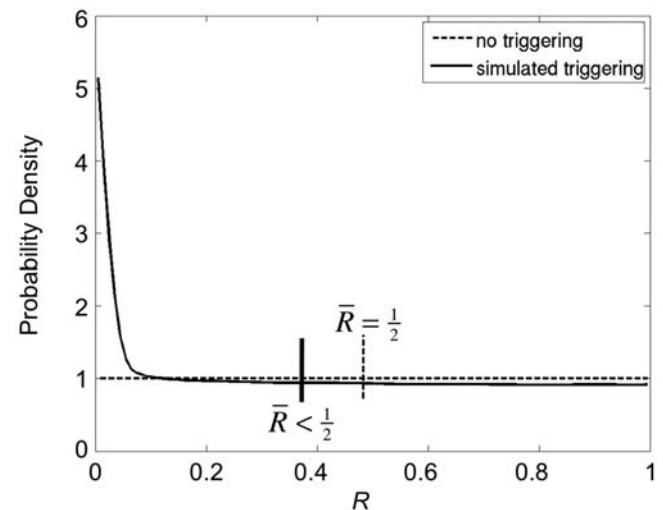

Figure 2. Schematic cartoon illustrating the distinction between the distribution of R in a case with no triggering (dashed) and a simulated case of strong triggering (solid). The integral of the probability density is 1 in both cases. The mean value of R is 0.50 in the nontriggered case and 0.46 in the triggered example.
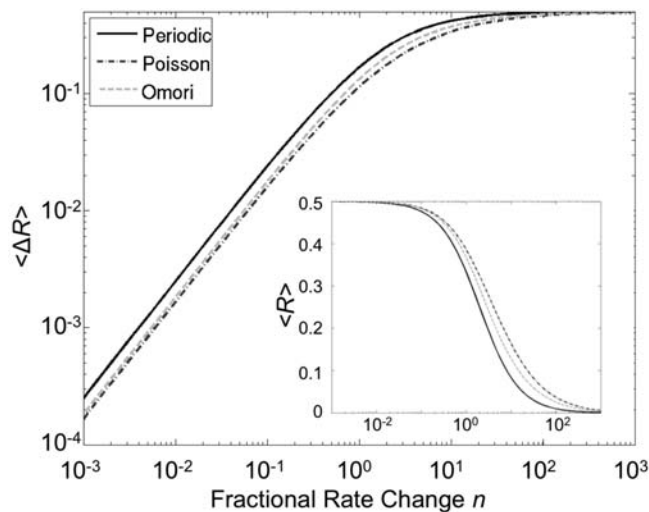
Figure 3. Expectation of R (equation (A10)), i.e., predicted $\overline{R}$, as a function of fractional rate change for three probabilistic models for earthquake occurrence, as described in the text. "Omori" refers to the nonhomogeneous Poisson model with Omori decay in triggered rate change. Inset shows the expectation of R on a linear-log scale, while the larger figure shows the value $\langle \Delta R \rangle = 0.5 - \langle R \rangle$ on a log-log scale to emphasize the scaling at small fractional rate changes, like those sought in this study. Fractional rate change is the normalized triggered earthquake rate defined in equation (3). The curves are all very similar, especially for small rate change.

characterized by a combination of Poisson distributed background earthquakes and triggered aftershocks that decay in time according to Omori's law [*Gardner and Knopoff*, 1974; *Hainzl et al.*, 2006; *Molchan*, 2005; *Saichev and Sornette*, 2006]. The time-decaying Omori's law component can be considered a nonhomogeneous Poisson process, that is, a Poisson process where the intensity is a function of time. This is a standard model for aftershock forecasting and is frequently used to analyze the significance of earthquake triggering metrics [*Kagan and Jackson*, 2000; *Marsan*, 2003; *Matthews and Reasenberg*, 1988; *Ogata*, 1999; *Reasenberg and Jones*, 1989; *Wiemer*, 2000]. We use it here to determine the expectation of R as a function of triggered rate change.

[17] Calculating the expectation of R for this nonhomogeneous Poisson process requires an estimate of the background rate and the parameters in Omori's law (Appendix A). These parameters may be heterogeneous in time and space and are impossible to determine for the single earthquakes that go into measurements of R. However, since we deal only with single earthquakes before and after the trigger, the details of the underlying interevent time distribution are relatively unimportant. Rather, we expect R to be primarily sensitive to average rates. This restricted sensitivity allows us to approximate the nonhomogeneous process as a simple stepwise homogeneous process, characterized by an average rate λ_1 before the trigger and a new average rate λ_2 afterward. For the stepwise homogeneous Poisson process, the expectation of R is given by (Appendix A)

$$\langle R \rangle = \frac{1}{n^2}[(n+1)\ln(n+1) - n], \qquad (2)$$

which is a function only of the normalized difference in average rate or fractional rate change,

$$n \equiv \frac{\lambda_2 - \lambda_1}{\lambda_1}. \qquad (3)$$

As anticipated, the expectation of R scales nonlinearly with rate change for the three models mentioned above: periodic, nonhomogeneous Poisson, and stepwise homogeneous (Figure 3). To emphasize the scaling for the small fractional rate changes, Figure 3 shows both the value of $\langle R \rangle$ and $\langle \Delta R \rangle \equiv 0.5 - \langle R \rangle$. The stepwise homogeneous model is found to be an excellent approximation of the more complex nonhomogeneous model, especially for the small rate changes we expect to deal with in this study. This demonstrates that the metric R is primarily sensitive to average seismicity rate change rather than the details of the interevent time model.

[18] As stated above, the nonlinearity in the scaling of $\overline{R}$ complicates the assessment of continuity between discontinuous far-field and near-field populations. We can address this complication by transforming the observations using equation (2) to map the measured $\overline{R}$ into a modeled fractional rate change n. That is, we can interpret the measured $\overline{R}$ in terms of the number of triggered earthquakes required to produce that $\overline{R}$. Although we had no a priori expectation for the scaling of $\overline{R}$ with dynamic strain, we do have an expectation for the scaling of n with dynamic strain. Studies of traditional aftershock zones have found that the number of aftershocks scales with main shock magnitude as $\log N \propto M$ [*Felzer et al.*, 2004; *Gasperini and Lolli*, 2006; *Helmstetter et al.*, 2005; *Ogata*, 1992; *Yamanaka and Shimazaki*, 1990]. Since peak ground velocity (a proxy for dynamic strain) also scales with magnitude as $\log PGV \propto M$, the aftershock scaling with magnitude is consistent with a power law scaling of aftershock rate with dynamic strain. Studies comparing aftershock rates directly to peak ground velocities suggest that aftershock rates may even be linearly proportional to dynamic strain, i.e., with a power law exponent of ~1 [*Gomberg and Felzer*, 2008]. If our probabilistic model (equation (2)) is adequate and assuming that at least the more conservative power law scaling hypothesis holds, then the transformed statistic n should scale linearly on a log-log scale. In section 4, we will show that this hypothesis is confirmed by the data. This gives us the tool we need to compare relative triggering rates in near-field and far-field populations.

[19] In what follows, we refer to n as triggering intensity to emphasize that it is a transformed statistic and not a direct measurement of fractional rate change. Nevertheless, equation (2) represents a smoothly continuous transformation, and therefore, the transformed statistic n should not scale continuously with dynamic strain amplitude unless the primary statistic $\overline{R}$ does so as well.

3. Defining Populations

[20] The statistic $\overline{R}$ (or the transformed statistic n) measures triggering intensity in a population of earthquakes. Therefore, the first step in applying the interevent time method to a real data set is to define reasonable populations so that we can evaluate the different rate changes in each one.

[21] Because long-range triggering is clearly associated with dynamic strain, we start by constructing sets of earthquakes with common dynamic strain amplitude. Other aspects of the seismic waves may be important in terms of triggering earthquakes, such as duration or frequency of the seismic waves. For instance, some studies suggest that higher-frequency waves are more effective triggers [*Gomberg and Davis*, 1996] while some attribute more triggering power to lower frequencies [*Brodsky and Prejean*, 2005]. Other studies find that frequency or number of oscillation cycles may modulate triggering power slightly, but these aspects are of secondary importance to peak amplitude [*Savage and Marone*, 2008]. Comparison between radial aftershock decay and ground motion attenuation at intermediate distances supports a scaling with peak or average ground velocities, independent of duration [*Gomberg and Felzer*, 2008]. Given the uncertainties regarding other aspects of the seismic waves, we choose to define populations based only on peak amplitude. Observed differences between near-field and far-field triggering intensities may therefore be attributed to second-order aspects of the wavefield and not only to other triggering agents such as static and postseismic strain.

[22] Peak dynamic strain is roughly proportional to the amplitude of seismic waves

$$\varepsilon \approx \frac{A}{\Lambda} \approx \frac{V}{C_S}, \tag{4}$$

where A is displacement amplitude, Λ is wavelength, V is particle velocity, and C_S is seismic wave velocity [*Love*, 1927]. In principle, dynamic strain can therefore be calculated wherever there is a seismogram. In this study, we use empirical ground motion regressions to approximate seismic wave amplitude, allowing us to extend strain estimates to any point on the map. Ground motions are converted to dynamic strain estimates by dividing by wavelength or wave speed, depending on whether the regression is for displacement or velocity, respectively.

[23] In the near field, S waves should carry the largest dynamic strains, with a dominant period on the order of 1 s [*Boatwright et al.*, 2001]. S wave velocity at seismogenic depths is roughly 3.5 km/s. In the far field, surface waves with periods near 20 s dominate ground motion, as smaller period waves tend to be scattered and attenuated [*Lay and Wallace*, 1995]. Both Love and Rayleigh waves can trigger earthquakes [*Hill*, 2008; *Velasco et al.*, 2008], but the 20 s Rayleigh wave, with a velocity of ~3.5 km/s, is usually associated with the surface wave magnitude equation we use to estimate peak ground motions [*Lay and Wallace*, 1995]. We therefore treat this phase as representative of far-field dynamic strains. We note that if triggering is in fact dominated by Love waves, with a velocity of ~4.3 km/s, equation (4) may overestimate strain by ~20% for equivalent amplitude waves.

[24] Previous work has investigated the accuracy of using ground motions as a proxy for dynamic strain at depth by comparing strain estimated from seismometer data to strain measured by strainmeters [*Gomberg and Agnew*, 1996]. This study found that although there was considerable deviation in observed strains from those expected for a simple layered earth model, the dynamic strain amplitudes calculated from ground motions generally agreed within ±20% of the strainmeter measurements for periods between ~10 and 25 s and within ±50% outside this band. These uncertainties are smaller than the factor of two uncertainties related to the empirical regressions used to estimate peak ground motions (see below). Since we are interested in the first-order scaling of triggering intensity with dynamic strain amplitude averaged over many earthquakes, we consider peak ground motions to be an adequate order-of-magnitude proxy for peak dynamic strains.

3.1. Estimating Dynamic Strain With Empirical Ground Motion Regressions

[25] In order to take full advantage of the large number of earthquakes in the catalog, we must calculate dynamic strain at any point on the map for any trigger in the catalog, not only where we have seismic stations and archived waveforms. We therefore use empirical ground motion regressions to estimate strain as a function of distance from the potential trigger earthquakes. Peak ground motions are well studied at near and intermediate distances for estimating seismic hazard and at regional and teleseismic distances for calibrating magnitude scales [*Abrahamson and Silva*, 2008; *Boatwright et al.*, 2003; *Campbell and Bozorgnia*, 2007; *Joyner and Boore*, 1981; *Lay and Wallace*, 1995; *Richter*, 1935]. However, published regressions rarely focus on the very near-field distances and small magnitudes of interest in this study and are insufficient for our purposes. Previous researchers comparing aftershock distribution to peak ground motions have performed their own regressions with an emphasis on the near field [*Gomberg and Felzer*, 2008]. We also perform our own small-magnitude, near-field peak ground velocity (PGV) regression, using California Shakemap data [*Wald et al.*, 1999]. *Boatwright et al.* [2003] also used Shakemap data to make an empirical ground motion regression, but used only a small subset of the data available today and did not focus on the small distances of interest in this study.

[26] For the near-field regression, we follow the Next Generation Attenuation study of *Campbell and Bozorgnia* [2007] and use an equation of the form

$$\log_{10} \mathrm{PGV} = c_1 + c_2 M - c_3 \log_{10} \sqrt{r^2 + c_4^2}, \tag{5}$$

where PGV is peak ground velocity (in cm/s), M is earthquake magnitude, r is hypocentral distance (in km), and c_i are fit parameters. The fit parameters are found by regression analysis using ~2000 PGV measurements from the Shakemap archives (Table 1). The details of the regression are given in Appendix B.

[27] For far-field dynamic strain, we use the surface wave magnitude relation [*Lay and Wallace*, 1995],

$$\log_{10} A_{20} = M_S - 1.66 \log_{10} \Delta - 2, \tag{6}$$

where A_{20} is in micrometers and Δ is in degrees. This equation is commonly used to assign a catalog magnitude based on measured amplitude at some distance. We turn the procedure around and use the catalog magnitude to calculate amplitude. This approach uses the long-period waves ($T = 20$ s) as indicators of the peak dynamic strain, implicitly assuming that the short-period body waves are attenuated at large distances. The displacement A_{20} is converted to velocity

Table 1. Best Fit Regression Constants for Equation (5)[a]

	c_1	c_2	c_3	c_4 (km)
Unconstrained	−2.29 (−2.79, −1.80)	0.85 (0.75, 0.96)	1.29 (1.58, 1.00)	0 (0, 0)
Constrained	−2.83 (−3.13, −2.56)	1	1.34 (1.59, 1.03)	0 (0, 0)

[a]Values in parentheses are 95% confidence limits from 1000 bootstrap resamplings of the underlying peak ground velocity data set. The regression always prefers $c_4 = 0$. The second row of constants is used in the ETAS simulation, in which case c_2 is constrained to equal 1 to match observed aftershock scaling.

for the 20 s waves by the approximation $V \approx 2\pi A_{20}/T$ [*Aki and Richards*, 2002]. Equation (6) was historically calibrated using a similar catalog of global earthquakes to the one we use for potential triggers and so provides a good measure of average amplitude despite being imperfect for any individual earthquake. The standard magnitude error for this regression, reflecting both interevent variations (e.g., source depth) and intraevent variations (e.g., radiation pattern), has been tabulated for a selection of seismic stations [*Rezapour and Pearce*, 1998], and we compute a pooled standard error of 0.28 units. Through equation (6), this corresponds to a factor of ~2 uncertainty in the estimated strain amplitude. The surface wave magnitude equation is designed for distances on the order of at least 800 km [*Lay and Wallace*, 1995], and this sets the minimum distance for the population of long-range triggers in this study.

3.2. Defining Populations Over Space

[28] A large far-field quake may trigger numerous earthquakes distributed throughout the study area. We therefore split the study region into spatial bins and calculate R for each of these bins (Figure 4). This generates a number of R values for each trigger and ensures that the measurements are not dominated by any single region with particularly high activity. Using a spatial bin that is much smaller than the wavelength of the long-range trigger also ensures that measured triggering intensity reflects the dynamic strain at that site. These R values are then pooled according to peak dynamic strain as calculated by equation (6) rather than according to their particular trigger. In this way, each strain bin incorporates numerous triggers at various combinations of distance and magnitude.
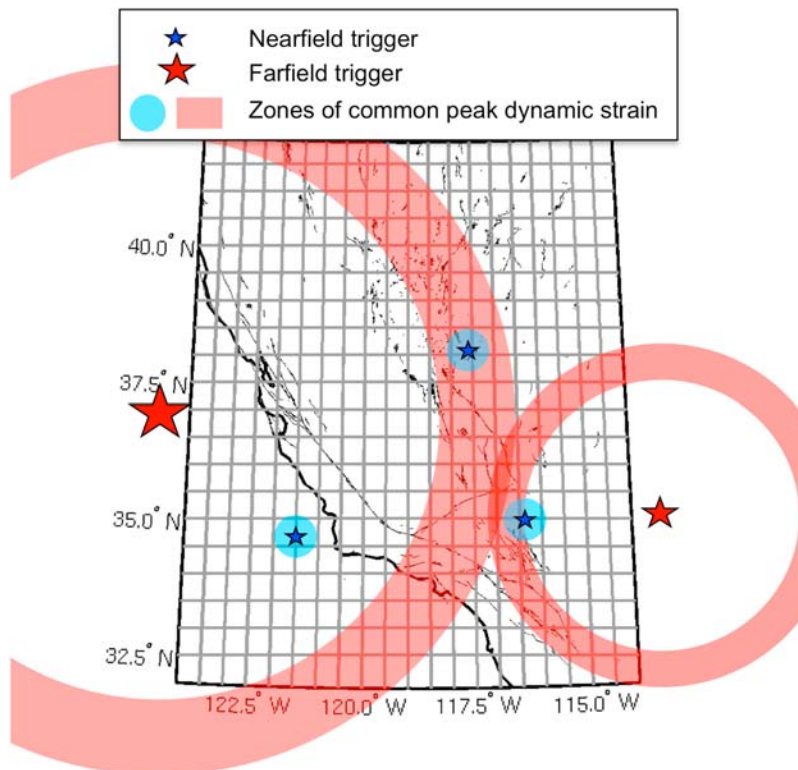

Figure 4. Cartoon illustrating the construction of earthquake populations for analysis with the interevent time method. For the long-range case (red), various combinations of magnitude and distance are combined to create populations of earthquakes bracketing potential triggers of common dynamic strain amplitude at the site of the triggered quakes. The study area is gridded, and the interevent time ratio R is calculated in each bin for each trigger. Zones of common dynamic strain form arcs within the study zone. For the short-range case (blue), populations are constructed by combining all earthquakes within some small radius of potential triggers of common magnitude. Spatial grid is not to scale.

[29] The higher the number of bins, the higher the number of bracketing pairs for each trigger quake, down to a lower size limit where single earthquakes begin to be isolated. A bin size of $0.1° \times 0.1°$ gives the maximum number of bracketing pairs for the whole catalog of potential triggers, but we perform the analysis using several different bin sizes to ensure robustness of the results with respect to parameter choices (section 6.3).

[30] To measure the time ratio R for near-field triggering, we search for the first earthquake before and after a potential trigger in a disk centered on the trigger earthquake epicenter. The radius of the disk is set to give the same area as in the far-field bins, e.g., for a far-field bin of $0.1° \times 0.1°$ we define the near-field radius as ~6.2 km. The time ratios R are then associated with the mean peak dynamic strain over the area of the disk. Assuming radial symmetry (i.e., approximating the trigger as a point source) and using equations (4) and (5), the average peak dynamic strain in the near-field disk is

$$\bar{\varepsilon} = \frac{\overline{PGV}}{C_S} = \frac{1}{C_S \pi D^2} \int_0^D PGV(r) 2\pi r \, dr, \qquad (7)$$

where C_S is shear wave velocity, $PGV(r)$ is given by equation (5), and D is the radius of the disk.

[31] We estimate the uncertainty in near-field peak dynamic strain by bootstrap resampling the Shakemap data directly, refitting the regression formula, and recalculating the mean peak strain according to equation (7). This is preferable to using the uncertainties in the regression constants themselves, because it accounts for strong correlations between the regression parameters. We resample 1000 times and report 95% confidence levels.

3.3. Earthquake Catalogs

[32] Using the interevent time method on earthquake populations requires large catalogs for both potential trigger earthquakes and for local seismicity. The trigger catalog is drawn from the global Advanced National Seismic System (ANSS) catalog from 1984 through April 2008. We choose the ANSS catalog because it includes both global earthquakes and local California earthquakes in a self-consistent catalog. More specialized regional or global catalogs may contain more carefully determined moment magnitudes and refined earthquake locations, but given the order of magnitude nature of our strain estimates, the small potential increase in accuracy is not worth the sacrifice in consistency.

[33] For the global catalog, a depth cutoff is imposed at 100 km, because deep earthquakes do not generate significant surface waves. Only earthquakes with surface wave amplitude greater than 10 μm displacement are treated as potential triggers. This minimum corresponds to a $M_S 4.5$ earthquake at 800 km. We find that this cutoff is sufficiently small to resolve an observational threshold for long-range triggering.

[34] Potential near-field triggers are drawn from the ANSS catalog for the California study region. Other regional catalogs have considerably smaller location errors than the ANSS catalog but contain considerably fewer earthquakes. However, location error should not be a significant source of error for this study, because the required spatial preci-

sion is on the order of the spatial bin size. We therefore choose the catalog with the largest number of earthquakes. The interevent time method should not be sensitive to regional variations in completeness magnitude, because the incompleteness should affect the pretrigger and posttrigger catalogs in a consistent way. However, we impose a magnitude threshold of 2.1, based on the roll-off in the Gutenberg Richter distribution for the catalog as a whole, to protect against large swings in completeness level with time. An upper magnitude cutoff is imposed to prevent the rupture length from exceeding the radius of aftershock collection. For a spatial bin size of $0.1° \times 0.1°$, this corresponds to a magnitude of about 5.5. The study area extends from 114° to 124° west and from 32° to 42° north.

[35] We also look at the scaling of triggering intensity with dynamic strain in Japan. Here we use the Japan Meteorological Agency (JMA) catalog from 1997 through March 2006. For consistency with California, we limit the catalog of local events to shallower than 15 km within the land area of the four main islands of Japan. The magnitude of completeness for the JMA catalog of shallow crustal earthquakes may be below 2.1, but we impose this larger magnitude cutoff for consistent comparison with California.

3.4. Practicalities of Implementation

[36] In order to evaluate the significance of $\bar{R}$ as an indicator of triggering, we require confidence bounds on $\bar{R}$. We use the bootstrap method to generate confidence bounds by randomly resampling the R distribution for a given population to generate a suite of estimates of $\bar{R}$ [Casella and Berger, 2002]. The confidence bounds on triggering intensity n are then calculated by applying the transformation (equation (2)) to the bounds computed for $\bar{R}$.

[37] We also take into consideration two potential sources of undesirable bias for realistic sets of earthquakes: (1) the superposition of Omori's law on measurements made in aftershock sequences and (2) the finiteness of the earthquake catalog. The reader should note that understanding these practicalities is important for implementing the interevent time method but is not crucial for understanding the results presented in subsequent sections.

[38] The superposition of Omori's law on the measurements is a significant issue for near-field triggering, but not far field, and thus could affect the two populations differently. Consider the three earthquakes shown in Figure 1. The metric R is designed to measure whether or not earthquake B affects the timing of earthquake C. However, for the near-field case, it is possible that earthquakes B and/or C are aftershocks of earthquake A. In this case, the times t_1 and t_2 are not uncorrelated. An Omori rate decay ($\sim t^{-1}$) is instead superimposed on the timing of both the trigger quake (quake B) and the subsequent quake. Measuring R in an aftershock sequence, where seismicity rates are decreasing, can spuriously associate the trigger with a seismicity rate decrease. On the other hand, the far-field population is not subject to this effect, as it is very unlikely that a distant earthquake B is an aftershock of a local earthquake A.

[39] Since the Omori's law bias only affects the near-field population of quakes, it could interfere with the comparison of triggering intensity between the populations. This bias is suppressed by requiring that any event treated as a
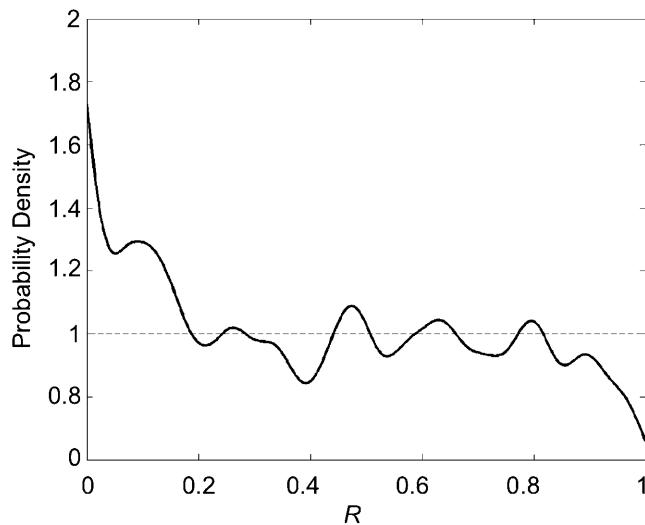
Figure 5. Distribution of R for the 2002 M7.9 Denali earthquake. Individual R values are computed in $0.1° \times 0.1°$ spatial bins. The high proportion of small R values demonstrates triggering in a large proportion of the bins. The mean of R is 0.475. Data are smoothed by a 0.09 unit cosine filter for clarity.

trigger (earthquake B) must be larger than the preceding local event (earthquake A). The condition ensures that the rate increase due to the trigger is much larger than any Omori's law rate decrease associated with the prior quake. A higher magnitude difference better ensures against bias at the cost of reducing the number of eligible trigger quakes. We find that $\overline{R}$ is stable for a magnitude difference of at least one unit. One magnitude unit corresponds to a roughly tenfold increase in total triggering power [*Reasenberg and Jones*, 1989], and Omori's law ensures that the difference is in general much greater than this, because the influence of the previous earthquake decays rapidly with time.

[40] The second potential source of bias is related to the finiteness of the catalog. This is especially problematic in regions where seismicity rates are low. To understand this effect, consider an ideal catalog with no triggering and uniformly distributed earthquake interevent times. Now consider a distant earthquake with a time near the beginning of the catalog as a potential trigger. Since there is no triggering in this hypothetical catalog, the times to the first earthquake before and after (t_1 and t_2) should be distributed identically, taking values between 0 and infinity, and $\overline{R}$ should be 0.5. However, for a finite catalog, larger values of t_1 and t_2 are missing, because they fall outside the bounds of the catalog. For our hypothetical trigger near the beginning of the catalog, we can only measure R when t_1 happens to be small enough to appear in the catalog, while t_2 can take much larger values and still make it into the catalog. This sampling bias causes $\overline{R}$ to differ from 0.5. The bias is unique for each spatial bin, as it depends on the particular combination of trigger times and the average seismicity rate in the bin.

[41] We compute this bias stochastically by determining $\overline{R}$ for 1000 simulated catalogs in which local earthquake occurrence times are replaced by uniformly distributed random times. The calculated bias is subtracted from the values of

$\overline{R}$ measured for the actual catalog. This means that, in effect, $\overline{R}$ is reported relative to a simulated control case with zero triggering. For simplicity, the bias-corrected mean is referred to below as $\overline{R}$.

[42] Correcting for the finite catalog bias somewhat reduces the apparent triggering for the far-field triggers but does not significantly alter the near-field data, presumably because near-field triggers tend to be located in regions with very high seismicity rates. The selection criteria for avoiding the Omori's law bias are only applied to the near-field triggers. We demonstrate that these bias corrections are adequate by applying the interevent time method to a simulated earthquake catalog in section 5. First, however, we show the results for the real seismicity catalogs.

4. Observed Triggering Intensity as a Function of Dynamic Strain

4.1. Proof of Concept: Denali

[43] We begin attacking real data by measuring the interevent times for a well-known case of pervasive triggering in order to establish that $\overline{R}$ and n behave as designed. The 2002 magnitude 7.9 Denali earthquake generated peak dynamic strains on the order of $2-3 \times 10^{-7}$ for the California study area, according to the empirical regressions, and is known to have triggered significant seismicity [*Gomberg et al.*, 2004; *Prejean et al.*, 2004]. For this initial case study, we disregard dynamic strain amplitude variations and define a population consisting of the full gridded study area. The resulting R distribution reflects significant triggering (Figure 5). The sample mean $\overline{R}$ (with 95% confidence limits) is 0.475 (0.461–0.488), corresponding to a fractional rate change n of 0.16 (0.08–0.26) according to equation (2). A simple earthquake count in the 24 h before and after the Denali earthquake indicates a 22% seismicity rate increase in the following 24 h. These estimates agree within error. We conclude that R is capable of capturing triggering in a case with known seismicity rate increases.

4.2. Triggering Intensity in the Full Catalog

[44] The real utility of the method becomes apparent when it is applied to the full ANSS data set with over 3000 potential far-field triggers and 12,000 near-field triggers meeting our criteria. Figure 6 shows measured R distributions for different dynamic strain amplitudes, corresponding to various combinations of magnitude and distance for the long-range data set and various magnitudes at constant distance for the short-range data. The distributions show evidence of both immediate triggering ($t_2 \sim 0$), in the form of large spikes at $R \approx 0$, and protracted or delayed triggering ($0 < t_2 < t_1$), in the form of a gradual decrease in probability density with increasing R. The distributions show larger proportions of small R for higher dynamic strain amplitudes, as expected.

[45] To assess whether the intensity of dynamic triggering in the far field can account for the observed intensity of triggering in the near field, we plot the sample mean $\overline{R}$ and the transformed triggering intensity n, calculated from equation (2), as a function of peak dynamic strain for both near-field and far-field populations (Figures 7a and 7b). To emphasize the scaling of $\overline{R}$ at small strains, Figure 7a shows the value $\Delta\overline{R} = 0.5 - \overline{R}$, as in Figure 3. Triggering intensity
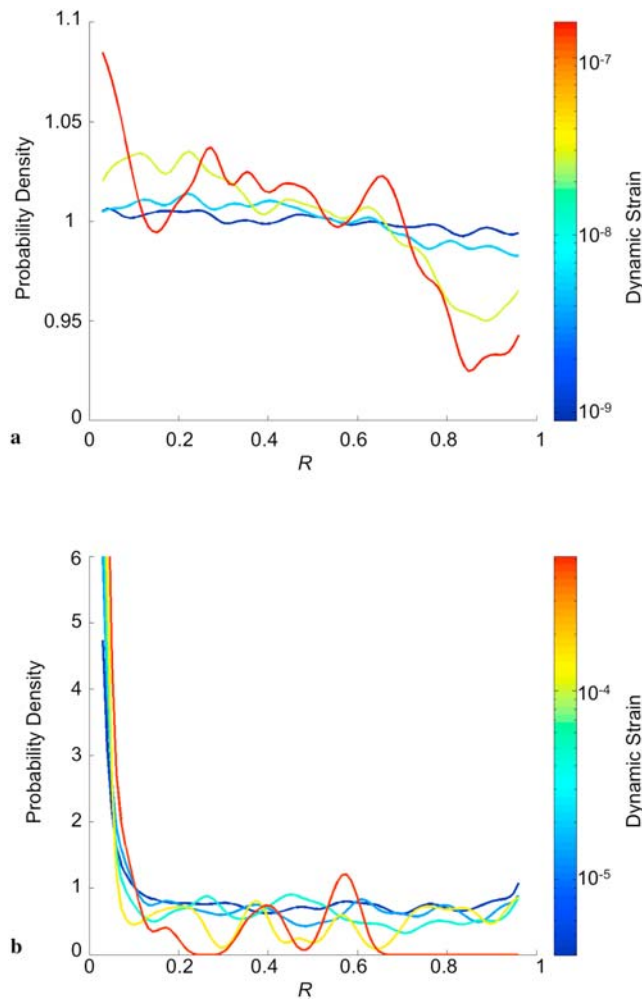
Figure 6. Empirical probability densities (distributions) for R. (a) Far-field California data (trigger distance > 800 km) for four dynamic strain increments. (b) Near-field data for magnitudes 3.1–5.1 in five increments. Curves have been smoothed for clarity using a cosine-weighted running average with a window width of 0.09 units. The oscillations at this wavelength are therefore a spurious effect of the smoothing. Curves are truncated at the limits to avoid plotting edge effects of the smoothing.

in the far field scales with the amplitude of peak dynamic strain. Comparing the triggering intensity for the near-field population to a trendline fit to the far-field data, we find that the far-field (dynamic) triggering relationship can account for roughly half of the near-field triggering intensity (Figure 7d).

Although triggering intensity is best interpreted as a qualitative measure of actual rate change, the relative values should be fairly robust. The uncertainty is large, but the hypothesis that both populations of triggered quakes are produced in simple proportion to peak dynamic strain can be rejected at the 95% confidence level. Nevertheless, the far-field triggering relationship accounts for a significant portion of the near-field aftershocks, accounting for about 60% of earthquakes within ~6 km of a $M3.1$ near-field trigger and about 15% within the same distance of a $M5.5$ trigger.

[46] We can define a dynamic triggering threshold in the far field as the smallest dynamic strain for which the 95% confidence limits on $\overline{R}$ fall above 0.5. By this definition, the dynamic triggering threshold in California is approximately 3×10^{-9} strain. Note that this threshold is not dependent on the transformation from $\overline{R}$ to triggering intensity n, because the significance is evaluated through bootstrap resampling of $\overline{R}$ itself. For a crustal shear modulus of 30 GPa, this corresponds to a dynamic stress of 0.1 kPa. This estimate is several orders of magnitude smaller than previously reported for dynamic triggering [*Brodsky and Prejean*, 2005; *Gomberg and Davis*, 1996; *Gomberg and Johnson*, 2005; *Stark and Davis*, 1996]. We attribute this improvement in sensitivity to the interevent time method, which can detect small rate changes by using large populations. The threshold is discussed in more detail below.

[47] We also apply the interevent time method to Japan, assuming that the near-field regression determined in California can be applied to shallow crustal earthquakes in Japan at these small distances. In Japan, the dynamic strains from the largest far-field earthquakes are large enough to overlap in amplitude with the smallest of the near-field triggers. Where the two populations overlap, we again find a small additional near-field component, though not at the 95% confidence level (Figure 7c). Unfortunately, the uncertainty ranges are too large to assess the relative contributions with any confidence.

[48] Triggering intensity in shallow crustal Japan (Figure 7c) is reduced relative to California in both the near-field and far-field populations, with a higher dynamic triggering threshold of 10^{-6} strain. The relative paucity of long-range triggering in Japan has been documented before [*Harrington and Brodsky*, 2006], but this study shows that the reduced triggering susceptibility extends to the near field, as well. This difference in triggerability may reflect the difference in tectonic style (compressive versus transpressive) between the two study areas.

4.3. Dynamic Strain Threshold

[49] The interevent time method resolves triggering at dynamic strains as low as 3×10^{-9}. Many faults are regu-

Figure 7. (a) The mean interevent time ratio $\overline{R}$, in terms of the deviation from the value in the absence of triggering ($\Delta \overline{R} = 0.5 - \overline{R}$). Compare to Figure 3. Long-range (>800 km) triggers are in red, and short-range triggers (<6 km) are in blue. Vertical and horizontal error bars are 95% confidence limits. The green point corresponds to the Denali earthquake. The red horizontal bar shows the 2σ uncertainty associated with the far-field peak ground motion estimates. Triggering intensity n ($\overline{R}$ transformed via equation (2)) as a function of peak dynamic strain in (b) California and (c) Japan. The black dashed line in Figures 7a and 7b shows the weighted least squares fit to the California far-field data, along with 95% confidence levels. The best fit curve for California is also shown in Figure 7c for comparison with Japan. (d) The fraction of near-field triggered quakes accounted for by the far-field scaling relationship. First and second error bars represent 64% and 95% confidence limits, respectively.

larly exposed to such small dynamic strain amplitudes without being triggered [*Spudich et al.*, 1995]. The scaling of $\bar{R}$ with dynamic strain may therefore best reflect the distribution of fault strengths. The very low triggering intensity at the threshold would then reflect the scarcity of faults so very near failure.

[50] The dynamic strain threshold is also smaller than tidal strain fluctuations [*Cochran et al.*, 2004; *Scholz*, 2003].
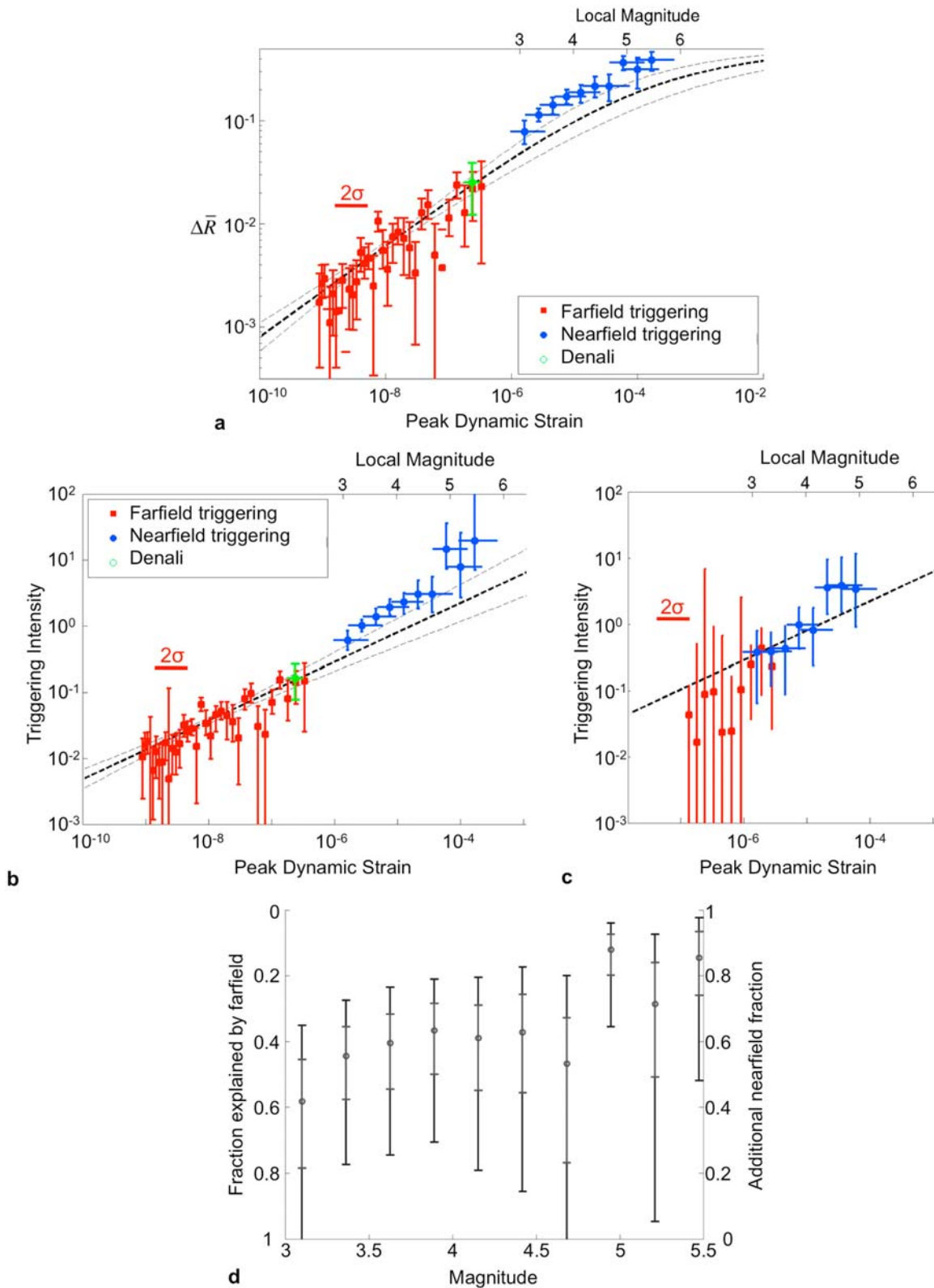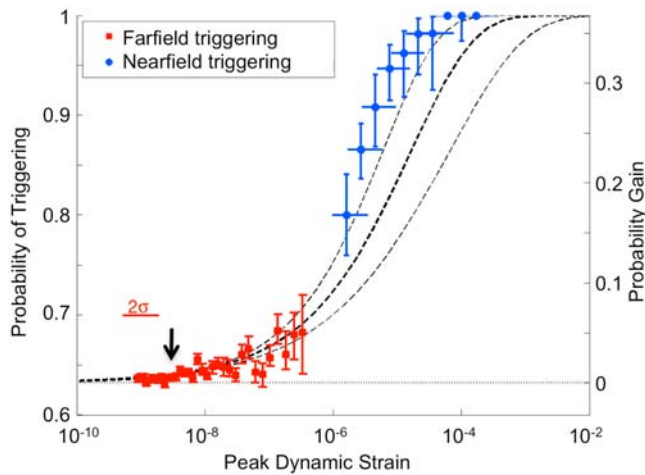

Figure 7

Figure 8. Probability of having an earthquake within the pretrigger recurrence interval (equation (8)) as a function of peak dynamic strain in California. Colors and error bars are as in Figure 7. The horizontal dotted line shows the baseline probability of having an earthquake within its own recurrence interval in the absence of triggering (~63%). The black dashed line is the best fit line from Figures 7a and 7b transformed using equation (8) and shows that the rapid increase in probability is consistent with a smooth increase in triggering intensity. The threshold for dynamic triggering (black arrow) is seen to be an observational threshold, with the probability of observed triggering going smoothly to zero with decreasing dynamic strain.

This is somewhat puzzling, because tidal strains might be expected to activate all available nucleation sites on a daily basis and set a lower limit for dynamic triggering. Strain tensors associated with crustal earthquakes are likely oriented with more variety than those due to the tides, however, and may access faults that tides are incapable of triggering. In addition, the forcing at the relatively long periods of the tides may be intrinsically different from the dynamic strains imposed at the short periods of seismic waves [*Beeler and Lockner*, 2003; *Gomberg et al.*, 1997; *Savage and Marone*, 2008].

[51] Evaluating the probability of triggering as a function of dynamic strain (Figure 8) aids in the interpretation of the observed triggering threshold. Probability is calculated from the triggering intensity n using the same Poissonian statistical model as before (Appendix C). This is not a new development, as the Poisson model is commonly used to transform an estimate of the number of triggered events into a probability of earthquake occurrence in a given time period [*Reasenberg and Jones*, 1989]. We discuss the probability of triggering in order to address (1) whether we would expect to resolve triggering below the threshold we have identified and (2) why previous studies may have failed to identify triggering at the very low levels identified here.

[52] The probability of triggering an earthquake within its own recurrence interval, as a function of n, is given by

$$P(N_{\text{EQs}} \geq 1) = 1 - \exp\{-(n+1)\}. \quad (8)$$

The baseline probability of having an earthquake in the absence of any rate change ($n = 0$) is ~63%. A positive n produces a positive probability gain. Figure 8 shows that the probability gain decreases smoothly to zero as n decreases. For the ~3×10^{-9} strain bin in California, there are ~10^5 interevent time measurements (~10^3 triggers × ~10^2 bins containing local earthquakes), and this number of events is sufficient to find $\bar{R}$ less than 0.5 at the 95% confidence level. We estimate (based on an assumed $\sqrt{n}$ scaling of the confidence bounds) that an order of magnitude more observations would be needed to push the observable threshold an order of magnitude lower. This exceeds the size of the earthquake catalog, and we infer that the absence of detected triggering at dynamic strains of less than 3×10^{-9} reflects an observational limit and not necessarily a physical threshold. If triggering occurs at lower dynamic strain amplitudes, we would not expect to resolve it.

[53] Understanding the probability of triggering also helps explain why previous studies have not identified dynamic triggering at the threshold reported here. Previous estimates of the dynamic triggering threshold have been based on waveform inspection, counting statistics, and/or likelihood methods. If triggering intensity $n > 1$, the change in seismicity rate is comparable to the background rate, and triggering is easily observable by inspection. Perhaps the conventional division between aftershocks and the more recently discovered far-field triggered populations results from the ease of observing large seismicity increases ($n > 1$) compared to the more subtle far-field triggering ($n < 1$). For a Poisson process, the variance is equal to the average rate, so $n > 1$ also roughly corresponds to the threshold for statistical significance using an earthquake count. Therefore, only the seismicity rate increases corresponding to $n > 1$, i.e., dynamic strains of nearly 10^{-5} are easily observable by these methods. Likelihood-based methods, in which triggered earthquakes are identified by determining whether the modeled likelihood of their occurrence is otherwise small, cannot resolve triggering where the triggering probability itself is very small. Figure 8 shows that the probability of observing a triggered earthquake does not exceed 5% below 10^{-6} dynamic strain. If triggering results in an additional earthquake fewer than 5% of the time, we cannot be 95% confident that the resulting earthquake count did not occur by chance. These considerations may explain why previous studies have not identified dynamic triggering at the level of 3×10^{-9} strain.

5. Validation and Calibration Through Statistical Seismicity Simulations

5.1. Effect of Triggering Cascades on the Measured Scaling of Triggering Intensity With Strain

[54] We have shown that triggering intensity scales with dynamic strain in both near-field and far-field populations, with a moderate additional component in the near field. However, there is a problem interpreting the quantitative slope of this trend. Previous work using earthquake counting and carefully declustered seismicity catalogs has shown that the number of local aftershocks following a main shock of magnitude M goes as $10^{\alpha M}$, with $\alpha \approx 1$ [*Felzer et al.*, 2004; *Helmstetter et al.*, 2005]. Since dynamic strain scales with magnitude as $\varepsilon \propto 10^M$ (equations (5) and (6)), this implies a
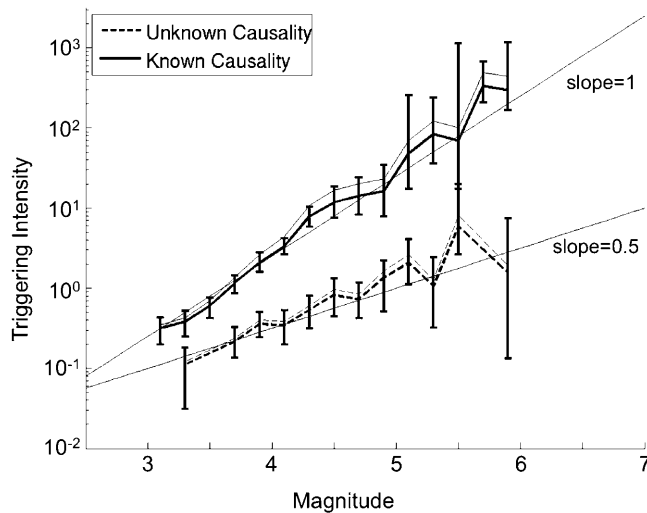
Figure 9. Testing the effect of the earthquake cascade on the transformation of $\overline{R}$ to triggering intensity n. A zero-dimensional (time only) ETAS model is used to generate a simulated seismicity catalog in which the triggering law and causal relationships are known. The nonhomogeneous transformation using Omori's law (thick lines) and the step-wise homogeneous transformation (thin lines) recover similar triggering intensities. If the interevent time ratio R is calculated using the first causally related earthquake before and after the trigger, the transformation recovers the imposed triggering law (solid curves). If the R calculation is not restricted to known causally related earthquakes (as occurs for real catalogs), the method recovers a reduced scaling exponent (dashed curves). Error bars are 95% confidence limits. Reference lines show a slope of 1 (the input relationship) and 0.5.

linear scaling of aftershock rate with peak dynamic strain. Studies comparing aftershock spatial decay directly to peak ground velocities also find aftershock rates to be consistent with a linear scaling with strain [*Felzer and Brodsky*, 2006; *Gomberg and Felzer*, 2008]. In contrast, this study suggests that triggering intensity varies with dynamic strain roughly as $n \propto \varepsilon^{0.5}$ in both populations (Figure 7b). We will now show that this discrepancy arises from the application of a probability model derived for isolated earthquake sequences to a catalog containing superimposed triggering cascades. In essence, the transformation fails to take into account that the interevent times are effectively sampled from two underlying distributions: the distribution of interevent times for triggered earthquakes and the distribution of times for background or uncorrelated quakes. The observed distribution of R is therefore a superposition of the two distributions illustrated in Figure 2. Fortunately, this effect can be quantified and calibrated using statistical simulations.

[55] As described in section 2.2, the sample mean $\overline{R}$ is transformed to triggering intensity n via a probabilistic model for earthquake occurrence times. This transformation is adequate for recovering the qualitative scaling of triggering rate change with dynamic strain amplitude. However, in order to recover absolute rates, we must employ a more sophisticated model that considers the effect of earthquake

cascades. The simple transformation from $\overline{R}$ to n implicitly assumed that we correctly associate earthquakes with their respective triggers, but a real catalog contains numerous superimposed triggering cascades. The first earthquake before and after a trigger may or may not then be causally related. If they belong to a different earthquake sequence, they will introduce R values sampled from a uniform distribution, and the resulting distribution will be some combination of the two curves illustrated in Figure 2. This has the effect of dampening the observed triggering signal.

5.2. Modeling Earthquake Cascades: Epidemic-Type Aftershock Sequence

[56] To evaluate whether the presence of superimposed earthquake cascades can explain the discrepancy between our recovered slope in Figure 7b and previous work based directly on earthquake counts, we generate an artificial earthquake catalog that follows the usually observed statistics of magnitude, timing, and triggering distributions (Appendix D). Because causality is known in the simulation, we can investigate how the use of the first earthquake before and after the trigger affects the recovered scaling relationship.

[57] A well-established method for generating such a catalog is the epidemic-type aftershock sequence (ETAS) [*Ogata*, 1992]. ETAS uses well-known empirical statistical seismicity laws as probability distributions to generate stochastic seismicity catalogs. Numerous researchers have used ETAS models to study the complex statistical repercussions of simple earthquake cascades [*Felzer et al.*, 2002, 2004; *Hardebeck et al.*, 2008; *Helmstetter and Sornette*, 2003; *Holliday et al.*, 2008]. Here we use ETAS to study the effects of superimposed earthquake triggering sequences on our transformation of $\overline{R}$ to an estimate of fractional rate change.

[58] We first apply the interevent time method to a zero-dimensional ETAS catalog. The zero-dimensional model simulates earthquakes in time only, disregarding spatial distribution, in order to isolate the effect of the earthquake cascade. The triggering law in the simulation corresponds to the case of the nonhomogeneous Poisson process with an Omori decay and the number of triggered earthquakes scales with $\alpha = 1$. We measure $\overline{R}$ for this simulated catalog using the first earthquake before and after each trigger (unknown causality) and also along individual branches of the triggering cascade (known causality). Both the stepwise homogeneous Poisson and the nonhomogeneous (Omori) model are then used to transform $\overline{R}$ to a triggered rate change.

[59] If interevent times are measured with respect to known branches of the cascade, i.e., if the causal relationships are known, the transformation from $\overline{R}$ to n recovers the scaling law that was put into the model (Figure 9). If we instead use the first earthquake before and after a putative trigger, a scaling with $\alpha = 0.5$ is recovered, similar to that recovered for the real catalog. This demonstrates that the discrepancy between our scaling and that found in other studies is due to the inclusion of some noncausally related interevent times in the R distribution. The simulation therefore suggests that our interevent time observations are consistent with the number of triggered earthquakes being directly proportional to dynamic strain, as found in previous studies. Consequently, the triggering intensity calculated by our transformation represents a lower bound on the real fractional rate change.

Table 2. Parameters Used in the ETAS Simulation, Representative of California[a]

	A	c (days)	p	κ (events km^{-2} strain^{-1})
Hardebeck et al. [2008]	0.008	0.095	1.34	454

[a]A is the productivity constant that controls the number of aftershocks per main shock, c is the time offset in the modified Omori's law, p is the time decay of aftershock rate in Omori's law, and κ is the productivity constant as a function of dynamic strain, calculated according to equation (D7).

[60] We have claimed that triggering intensity n serves as a good qualitative measure of the scaling with dynamic strain amplitude as long as it scales in a consistent manner with $\overline{R}$. The zero-dimensional simulation shows that n indeed scales consistently, but the zero-dimensional simulation only considered near-field aftershock triggering, not triggering from distant earthquakes unconnected to the local earthquake cascade. It is possible that the effect of unknown parentage will be different in the near field and far field. Since our conclusions about the relative contribution of dynamic strains in triggering near-field earthquakes is based on a projection of the far-field relationship into the near field, we need to confirm that the two populations are affected identically, despite the imperfect transformation to modeled rate change (i.e., equation (2)).

5.3. Space-Time ETAS Simulation

[61] To verify the robustness of the comparison between populations, we apply the interevent time method to a simulated earthquake catalog in which earthquakes are produced in simple proportion to peak dynamic strain at all distances. If the interevent time method recovers a continuous trend between the simulated near-field and far-field populations, we can then interpret the observed offset between the real populations as reflecting an additional near-field triggering component.

[62] To appropriately represent the two populations defined in this study, we use a full space-time simulated ETAS catalog (Appendix D). We make a key modification to the model, introducing far-field triggering in direct proportion to dynamic strain, as calculated from the empirical ground motion regression in equation (6). We also modify the near-field triggering rules to reflect the empirical PGV constants in equation (5). This requires very minor adjustments of published ETAS parameters. In order to match the known scaling of aftershock productivity with main shock magnitude, we set the regression constant $c_2 = 1$. This produces a negligibly larger misfit than the unconstrained PGV regression and does not significantly change the spatial decay (Table 1). This allows us to generate both near-field aftershock triggering and long-range triggering from distant sources with a consistent triggering rule.

[63] Applying the interevent time method, we recover a continuous trend for a representative set of ETAS parameter taken from the literature (Table 2 and Figure 10). This verifies that the method is capable of qualitatively measuring triggering in an ideal catalog with triggering proportional to strain. We are therefore justified in interpreting the offset in near-field and far-field triggering as reflective of an additional near-field triggering process.

[64] In section 5.2, we found that the transformation from $\overline{R}$ to triggering intensity n underestimates the actual productivity scaling α because of the superposition of triggering cascades. In the space-time ETAS simulations, we find that the slope of the trend is also reduced relative to the input value and varies slightly for different simulation runs, perhaps correlating with the fraction of triggered versus background earthquakes in a particular realization. The precise relationship between the absolute value of n and the other statistics of the catalog is beyond the scope of this study.

6.   Discussion

6.1.   Implications for Dynamic Triggering

[65] Triggering intensity scales with peak dynamic strain in the far field. Triggering in the far field (further than 800 km) can be confidently attributed to a dynamic agent, because the triggered earthquakes are well beyond the several source dimensions affected by static and postseismic stresses and the waiting times to the first triggered earthquakes are much less than the ~10 years required to propagate stresses viscously to these distances, as discussed in section 1. The empirical proportionality between dynamic strain and triggering intensity can account for a significant portion of triggering in the near field, but not all. Additional near-field triggering may reflect any or all of the following factors:
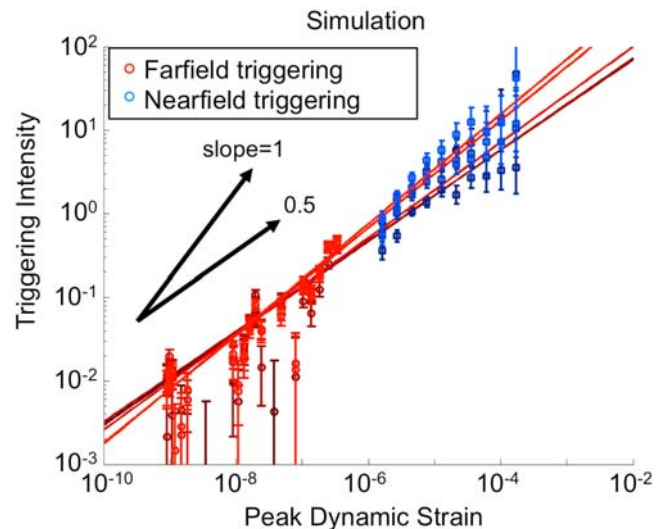

Figure 10. Triggering intensity n, determined by the interevent time method, plotted as a function of peak dynamic strain for simulated seismicity catalogs. Triggering is simulated as an identical function of peak dynamic strain in both near-field (blue hues) and far-field (red hues) populations. Different point brightnesses correspond to different simulation realizations. The recovery of a continuous trend between near-field and far-field populations validates the method and demonstrates that the offset in the observed trend (Figure 7b) can be confidently interpreted as reflecting an additional near-field triggering component. Lines of slope = 1 (the input relationship) and slope = 0.5 are plotted to show that the recovered scaling is again reduced relative to the input.

(1) the effect of prolonged static or postseismic strain near the main shock, (2) a dependence on frequency content where higher-frequency dynamic waves are more effective triggers, or (3) the concentration of potential nucleation sites (e.g., secondary fault strands, damage zones) in the regions very near to main shocks. If the near-field triggering component reflects static stress triggering, then this observation suggests that dynamic and static strains produce roughly equivalent numbers of earthquakes in the near-field of intermediate-magnitude earthquakes. Therefore, both effects must be taken into account to explain aftershock numbers and spatial distributions.

[66] It is important to note that the interevent time measurements do not simply reflect unusual behavior at the beginning of aftershock sequences. In fact, for small near-field triggers near the magnitude of completeness, the first triggered event is often the only aftershock in the sequence. Furthermore, stacked sequences consisting of only the first aftershocks of small main shocks follow the same Omori's law decay as single aftershock sequences of large main shocks [*Felzer et al.*, 2004; *Felzer and Brodsky*, 2006]. This implies that there is no physical distinction between the first cataloged aftershock and subsequent aftershocks in a sequence.

[67] How do dynamic strains, which produce no permanent load change, nonetheless account for a significant portion of near-field triggering? The low threshold for dynamic triggering suggests that arbitrarily small dynamic strains can trigger earthquakes on nucleation sites that are sufficiently near failure. Without a physical threshold for dynamic triggering, the question is one of a balance of two time scales, the time scale over which a nucleation site is loaded to failure quasi-statically versus the time between dynamic strain events large enough to push the fault the rest of the way. If the dynamic trigger recurrence time is smaller than the quasi-static time to failure, the fault will be triggered dynamically. A fault far from failure is unlikely to be triggered by any but the largest dynamic strain events. However, as the fault nears failure, not only are smaller and smaller dynamic strains required for triggering, but the availability of sufficient triggers increases due to the greater abundance of small earthquakes.

[68] In fact, a simple scaling argument shows that a fault is just as likely to be triggered by a small dynamic strain event as by a large one. The ETAS models show that the data are consistent with the number of dynamically triggered earthquakes being linearly proportional to dynamic strain. The number of earthquakes triggered by an earthquake of magnitude M therefore goes roughly as $\sim 10^M$. The Gutenberg-Richter distribution gives that the number of earthquakes with magnitude M goes as $\sim 10^{-M}$. Therefore, the total triggering power for each magnitude bin as a whole is constant,

$$N = N_{\text{Triggers}} \times N_{\text{Triggered}} = 10^{-M} \cdot 10^M = \text{constant.} \quad (9)$$

Small-amplitude triggers and earthquakes with magnitudes below the level of catalog completeness are therefore very important in triggering subsequent earthquakes. Similar arguments for the importance of small earthquakes have been made previously based on statistical considerations [*Felzer*

et al., 2004; *Felzer and Brodsky*, 2006; *Helmstetter et al.*, 2005; *Sornette and Werner*, 2005a, 2005b].

[69] The low observational threshold and the linear relationship between triggering intensity and dynamic strain amplitude place constraints on the mechanics of triggering. For example, these observations are not consistent with the exponential dependence between stress/strain and the number of triggered earthquakes predicted by classical rate and state friction [*Brodsky*, 2006; *Dieterich*, 1994; *Gomberg*, 2001]. The simplest way to reproduce the far-field observations may be to invoke a population of nucleation sites with a uniform distribution of dynamic triggering thresholds and a Coulomb-type nucleation criterion.

6.2. How Delayed Earthquakes Can Be Triggered Earthquakes

[70] Studies frequently identify only those earthquakes occurring during the passage of seismic waves as dynamically triggered. In applying the interevent time technique, we include arbitrarily delayed "first" earthquakes after the trigger. This inclusion is based on several considerations.

[71] First, the designation of an earthquake as "first" is a threshold-dependent, observational distinction. For a lower catalog detection threshold, we should always be able to find an earlier quake. This consideration is especially important for near-field triggering, where the detection threshold can be temporarily elevated and a tremendous number of early aftershocks are usually missing from earthquake catalogs [*Kagan*, 2004; *Peng et al.*, 2007]. Operationally, it is impossible to distinguish between primary, secondary, and delayed triggered earthquakes, as they share identical space, time, and magnitude statistics [*Brodsky*, 2006; *Felzer et al.*, 2004; *Kagan*, 2004]. Regardless, the rates of all of these classifications of earthquakes should be correlated, and secondary or delayed triggered earthquakes should reflect the intensity of the primary triggering process.

[72] Second, we wish to allow for the possibility that dynamic strains can trigger earthquakes by inducing a semipermanent change in the properties of the fault patch, rather than only through transiently exceeding the fault strength. Several studies have identified or posited long-lasting changes in the mechanical properties or effective stresses within fault zones related to the passage of high-amplitude seismic waves [*Brodsky et al.*, 2003; *Elkhoury et al.*, 2006; *Johnson and Jia*, 2005; *Parsons*, 2005; *Taira et al.*, 2009]. Delayed triggering may then simply reflect the prolonged nature of the triggering process.

[73] Regardless of whether delayed triggering reflects an incompletely observed earthquake cascade or a prolonged physical perturbation of the fault conditions, the inadvertent inclusion of uncorrelated (nontriggered) events will not invalidate the interevent time method, because these interevent times are drawn from a uniform distribution of R values and will not impart a false positive bias.

6.3. Robustness of the Observations With Regard to Parameters

[74] The binning of the data and the separation of triggered quakes into far-field and near-field populations required the introduction of arbitrary parameters. We want to be certain that our conclusions are robust with respect to these parameter choices. The success of the method in
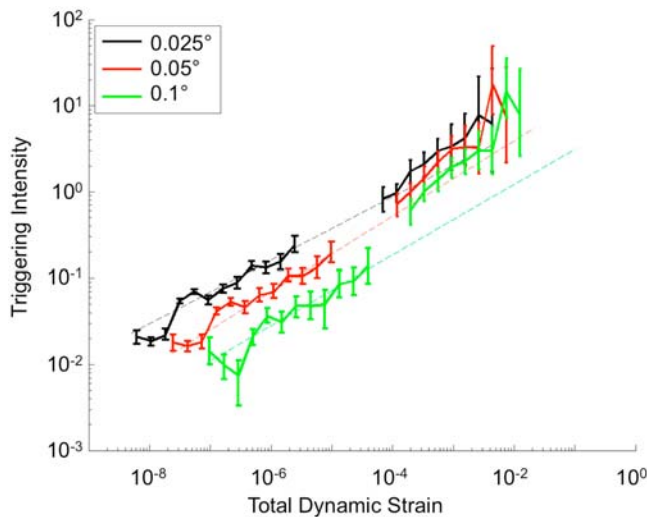
Figure 11. Triggering intensity as a function of dynamic strain for different bin sizes. Curves on the left are far-field data; curves on the right are near-field. The legend gives the far-field spatial bin dimension in degrees for each curve. The near-field aftershock radius is scaled to cover the same area as the far-field bins. For clarity of presentation, data are plotted against the peak dynamic strain integrated over the bin rather than the averaged dynamic strain and are therefore offset. The slopes of the curves and the absolute values of the triggering intensity change slightly with bin size, but the offset between trends is robust.

intensity with dynamic strain. Previous work has shown the relevance of dynamic triggering in the near field by comparing the falloff in aftershock density away from a main shock to the falloff of seismic waves at near and intermediate distances [*Felzer and Brodsky*, 2006; *Gomberg and Felzer*, 2008]. These correlations cannot be trivially mapped to a particular function of dynamic strain, however, because the decay in triggering intensity is superimposed on the decay of available nucleation sites away from the main shock. It is therefore necessary to carefully analyze the statistics of nontriggered (background) seismicity in order to extract the triggering function. The method defined here does not suffer from this ambiguity with respect to a background distribution, because each value of R reflects the seismicity rate change at a single site. We therefore do not need to be concerned about the geometry of the local fault network.

7. Conclusion

[79] The observations presented here have the following implications: far-field triggering scales with peak dynamic strain. This scaling, projected into the near field, accounts for 15%–60% of earthquakes within 6 km of magnitude 3–5.5 earthquakes. The additional near-field triggering component may reflect static stress triggering, frequency dependence for dynamic triggering, or concentration of nucleation sites very near main shocks. Extremely small dynamic strains can trigger faults if they are sufficiently near failure,
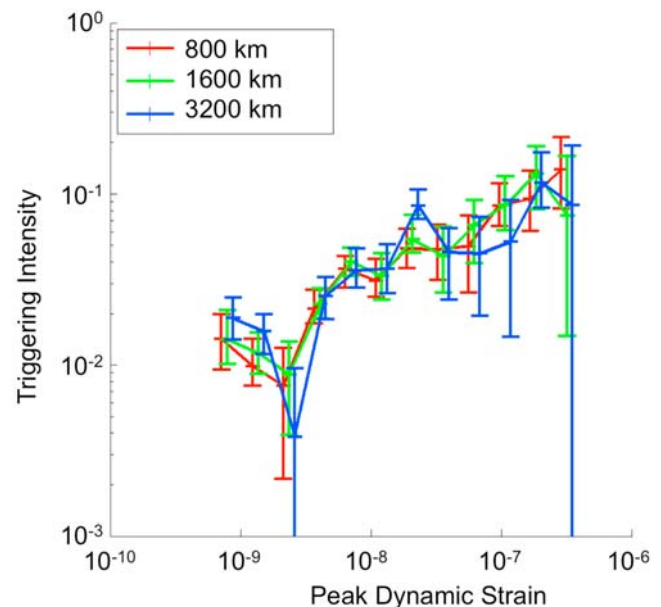
recovering a continuous trend for a control case using a simulated catalog with a continuous triggering law is a good confirmation, but we also check the robustness of the observations with respect to the data selection parameters.

[75] The first arbitrary parameter is the spatial bin size. The results shown in Figures 7–8 use a bin size of 0.1°, because this maximizes the number of R values we can calculate. Figure 11 confirms that the measurements are not sensitive to the spatial bin size, as long as the number of data points remains high. We show results for bin sizes between ~8 and 123 km^2 (0.025°–0.1° on a side). For larger bins, either the reduced quantity of data or the masking of triggered activity by unrelated local aftershocks causes confidence limits to exceed the mean triggering signal.

[76] The distance cutoff for far-field triggers also does not influence the results. Trials using minimum far-field cutoff distances of 800 km through 3200 km all recover essentially the same far-field scaling (Figure 12).

[77] Finally, to make sure the long-range triggering signal is not generated entirely by isolated geothermal areas, we plot the contribution of each spatial bin to the total measured triggering intensity, combining all the far-field amplitude bins (Figure 13). Geothermal regions (particularly Long Valley and Salton Trough) contribute strongly, but virtually all regions of active seismicity in California contribute to the long-range triggering signal.

6.4. Relation to Previous Work

[78] Dividing earthquakes into populations with common strain is a novel way of looking at the scaling of triggering

Figure 12. Sensitivity to long-range trigger cutoff distance for the California data set. The legend gives the minimum distance used for potential far-field trigger earthquakes. Results are not sensitive to distance cutoffs above 800 km, although uncertainties grow larger because of the reduced catalog size for larger cutoffs. We do not investigate distance cutoffs below 400 km, because the surface wave magnitude relation (equation (6)) is not appropriate for such small distances.
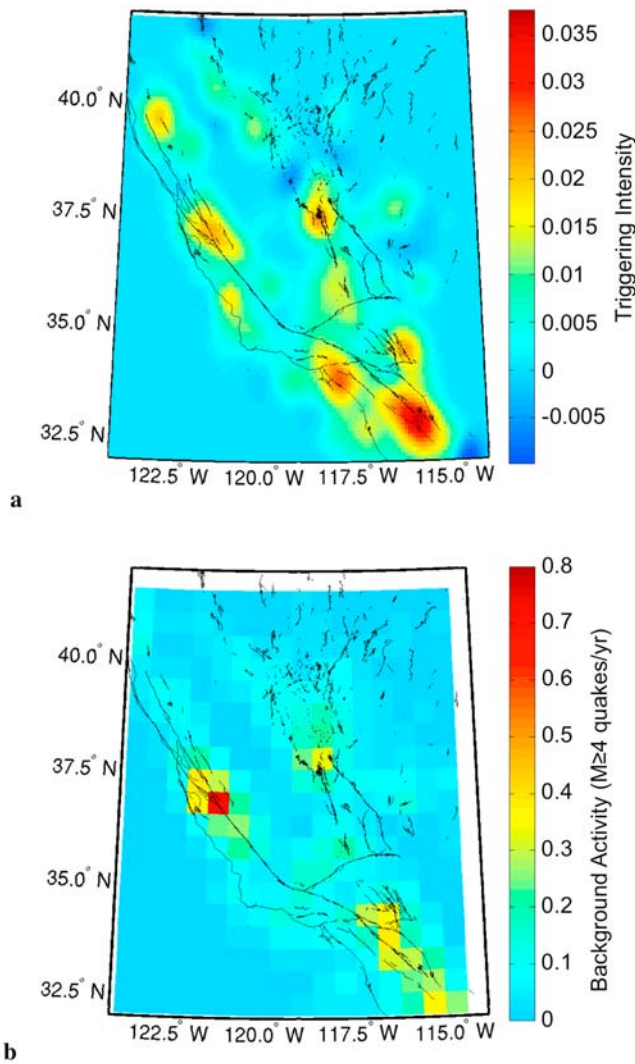
Figure 13. The geographical distribution of triggering susceptibility in California partially reflects the background activity rate. (a) Triggering intensity in 0.1° spatial bins for dynamic strains above 10^{-9}. (b) Background seismicity rate [*Hardebeck et al.*, 2008], expressed in terms of the number of magnitude 4 and greater earthquakes per year in each ~0.5° bin. The plots are qualitatively similar, implying that all regions of active seismicity are triggerable and no single region dominates the triggering signal. Both maps are smoothed by a 0.3° Gaussian kernel.

down to the observed level of 3×10^{-9} dynamic strain. ETAS simulations in which earthquakes are produced in direct proportion to dynamic strain reproduce the observed scaling of triggering intensity versus strain, suggesting that dynamic triggering intensity is linearly proportional to peak dynamic strain amplitude. This places a useful constraint on models for earthquake triggering mechanisms.

Appendix A: Expectation of R for a Poisson Process With a Step Change in Intensity

[80] To find the expectation of the interevent time ratio R as a function of rate change, we first derive the distribution

of R using an assumed distribution of interevent times t_1 and t_2 based on a probabilistic model. As discussed in the text, the most widely accepted model for the interevent time distribution is the nonhomogeneous Poisson process. We approximate this model with a stepwise homogeneous process. In a homogeneous Poisson process, events occur randomly in time with some average rate λ, known as the intensity. If the intensity λ is independent of time, the interevent times follow an exponential distribution,

$$f(t) = \lambda \exp\{-\lambda t\}. \tag{A1}$$

In a nonhomogeneous Poisson process, the intensity λ is a function of time and the interevent times are distributed as

$$f(t) = \lambda(t) \exp\left\{-\int_0^t \lambda(\tau) d\tau\right\}, \tag{A2}$$

where $\lambda(t)$ is the intensity at time t. The term within the exponential in both cases is the expected number of events at time t. We define the expected number of events $N(t)$ as

$$N(t) \equiv \int_0^t \lambda(\tau) d\tau \tag{A3}$$

for use in subsequent equations.

[81] The joint distribution of two independent interevent times is the product of two exponential distributions,

$$f(t_1, t_2) = \lambda_1(t_1)\lambda_2(t_2) \exp\{-N_1(t_1) - N_2(t_2)\}, \tag{A4}$$

where the subscripts 1 and 2 refer to intensities and times before and after the trigger, respectively. We derive the joint distribution of R (equation (1)) and a dummy variable $T = t_2$ by substituting these variables into equation (A4) and multiplying by the absolute value of the Jacobian of the variable transformation [*Casella and Berger*, 2002; *Walpole and Myers*, 1989]. Expressed in terms of R and T,

$$t_1 = \frac{T}{R} - T,$$
$$t_2 = T. \tag{A5}$$

The Jacobian of the transformation can be thought of as describing how areas under the distribution are expanded or contracted through the transformation. It is given by

$$J = \det\begin{pmatrix} \partial t_1 / \partial R & \partial t_1 / \partial T \\ \partial t_2 / \partial R & \partial t_2 / \partial T \end{pmatrix} = \det\begin{pmatrix} -\dfrac{T}{R^2} & \dfrac{1}{R} - 1 \\ 0 & 1 \end{pmatrix} = -\dfrac{T}{R^2}. \tag{A6}$$

The joint distribution for R and T is then

$$f(R, T) = \lambda_1\left(\frac{T}{R} - T\right)\lambda_2(T) \exp\left\{-N_1\left(\frac{T}{R} - T\right) - N_2(T)\right\}\left|-\frac{T}{R^2}\right|. \tag{A7}$$

The marginal distribution of R is obtained by integrating equation (A7) with respect to T,

$$f(R) = \int_0^\infty \lambda_1\left(\frac{T}{R} - T\right)\lambda_2(T)\exp\left\{-N_1\left(\frac{T}{R} - T\right) - N_2(T)\right\}\frac{T}{R^2}\,\mathrm{d}T.$$

(A8)

The expectation of R is defined as

$$\langle R \rangle = \int_0^1 Rf(R)\,\mathrm{d}R.$$

(A9)

Substituting equation (A8) into equation (A9) gives

$$\langle R \rangle = \int_0^1\int_0^\infty \lambda_1\left(\frac{T}{R} - T\right)\lambda_2(T)\exp\left\{-N_1\left(\frac{T}{R} - T\right) - N_2(T)\right\}$$
$$\cdot\frac{T}{R}\,\mathrm{d}T\mathrm{d}R.$$

(A10)

For an otherwise homogenous Poisson process with a step change in intensity λ, the solution to equation (A10) is

$$\langle R \rangle = \frac{\lambda_1\lambda_2}{(\lambda_2 - \lambda_1)^2}\left(\frac{\lambda_1}{\lambda_2} + \ln\left(\frac{\lambda_2}{\lambda_1}\right) - 1\right).$$

(A11)

Let us now define the fractional rate change as the number of triggered earthquakes in some posttrigger time interval normalized by the number that would be expected for the pretrigger rate,

$$n \equiv \frac{N_2(t) - N_1(t)}{N_1(t)}.$$

(A12)

For the stepwise homogeneous Poisson process, where λ_1 and λ_2 are each independent of time, this becomes

$$n = \frac{\lambda_2 - \lambda_1}{\lambda_1}.$$

(A13)

The expectation of R for the stepwise homogeneous process (equation (A11)) can then be rewritten solely as a function of fractional rate change n,

$$\langle R \rangle = \frac{1}{n^2}[(n+1)\ln(n+1) - n].$$

(A14)

Equation (A14) is equation (2) in the main text with the parameter n identified as triggering intensity. The sample mean $\overline{R}$ is transformed to triggering intensity n by equating $\overline{R}$ with the expectation $\langle R \rangle$ and solving numerically for n.

[82] We can also calculate the expectation of R for the nonhomogeneous (Omori-decaying) Poisson process, given an estimate of the parameters in Omori's law. In this case, the posttrigger rate is given by

$$\lambda_2(t) = \lambda_1 + \frac{k}{(t + c)^p}.$$

(A15)

The number of expected events as a function of time is then

$$N_2(t) = \lambda_1 t + \frac{k}{1 - p}\left[(t + c)^{1-p} - c^{1-p}\right],\ p \neq 1$$
$$N_2(t) = \lambda_1 t + k\ln\left(\frac{t}{c} + 1\right),\ p = 1.$$

(A16)

Substituting these definitions of λ_2 and N_2 into equation (A10), we integrate numerically to find the expectation of R.

[83] The transformation from observed $\overline{R}$ to fractional rate change n with the nonhomogeneous Poisson process is carried out by iteratively solving for the parameter k through equation (A10) and then calculating the fractional rate change n (equation (A12)) using equation (A16) for $N_2(t)$. A natural time scale for calculating n is $t = \lambda_1^{-1}$, the expected time to the first event given the pretrigger rate λ_1. The definition of fractional rate change n for the nonhomogeneous model then reduces to

$$n = \frac{k}{1 - p}\left[\left(\lambda_1^{-1} + c\right)^{1-p} - c^{1-p}\right],\ p \neq 1$$
$$n = k\ln\left(\frac{1}{c\lambda_1} + 1\right),\ p = 1.$$

(A17)

In this case, we need to estimate a representative background rate, as well as the Omori's law parameters. The fractional rate change recovered using equation (A17) is very similar to that recovered by the stepwise homogeneous transformation, as reflected by Figure 3.

Appendix B: Shakemap Peak Ground Velocity Regression

[84] We begin with an equation modified from the Next Generation Attenuation study of *Campbell and Bozorgnia* [2007],

$$\log_{10}\mathrm{PGV} = c_1 + c_2 M - c_3\log_{10}\sqrt{r^2 + c_4^2},$$

(B1)

where PGV is peak ground velocity (in cm/s), M is earthquake magnitude, r is hypocentral distance (in km), and c_i are fit parameters. This is equation (5) in the main text. This equation differs from *Campbell and Bozorgnia* [2007] only in the lack of magnitude dependence for the attenuation with distance. We also try a functional form that includes an exponential attenuation term but find that attenuation is negligible at the small distances studied.

[85] The regression data set consists of peak velocities from seismic stations within 15 km hypocentral distance from all California earthquakes having an archived Shakemap (http://earthquake.usgs.gov/earthquakes/shakemap). As of November 2009, this constitutes just over 2000 PGV measurements, with 140 within the ~6.2 km range defined as the near field in this study. PGV is corrected to hard rock values following the Shakemap methodology, which uses NEHRP site classifications based on shallow shear wave velocity [*Wald et al.*, 2006, section 2.4.3]. Data flagged as outliers during the generation of the Shakemaps are excluded. Since Shakemaps are generated very rapidly after a quake, earthquake magnitudes and locations listed in the Shakemap archive are often preliminary. Earthquake magnitudes and locations are therefore taken from the ANSS catalog for California, which combines locations from both northern and southern California seismic networks and is a more authoritative source. To reduce the potential impact of errors in earthquake locations, only data from earthquakes with catalog depths of at least 2 km are considered.

[86] A MATLAB nonlinear optimization algorithm (FMIN-CON) is used to solve for the constants in equation (B1),
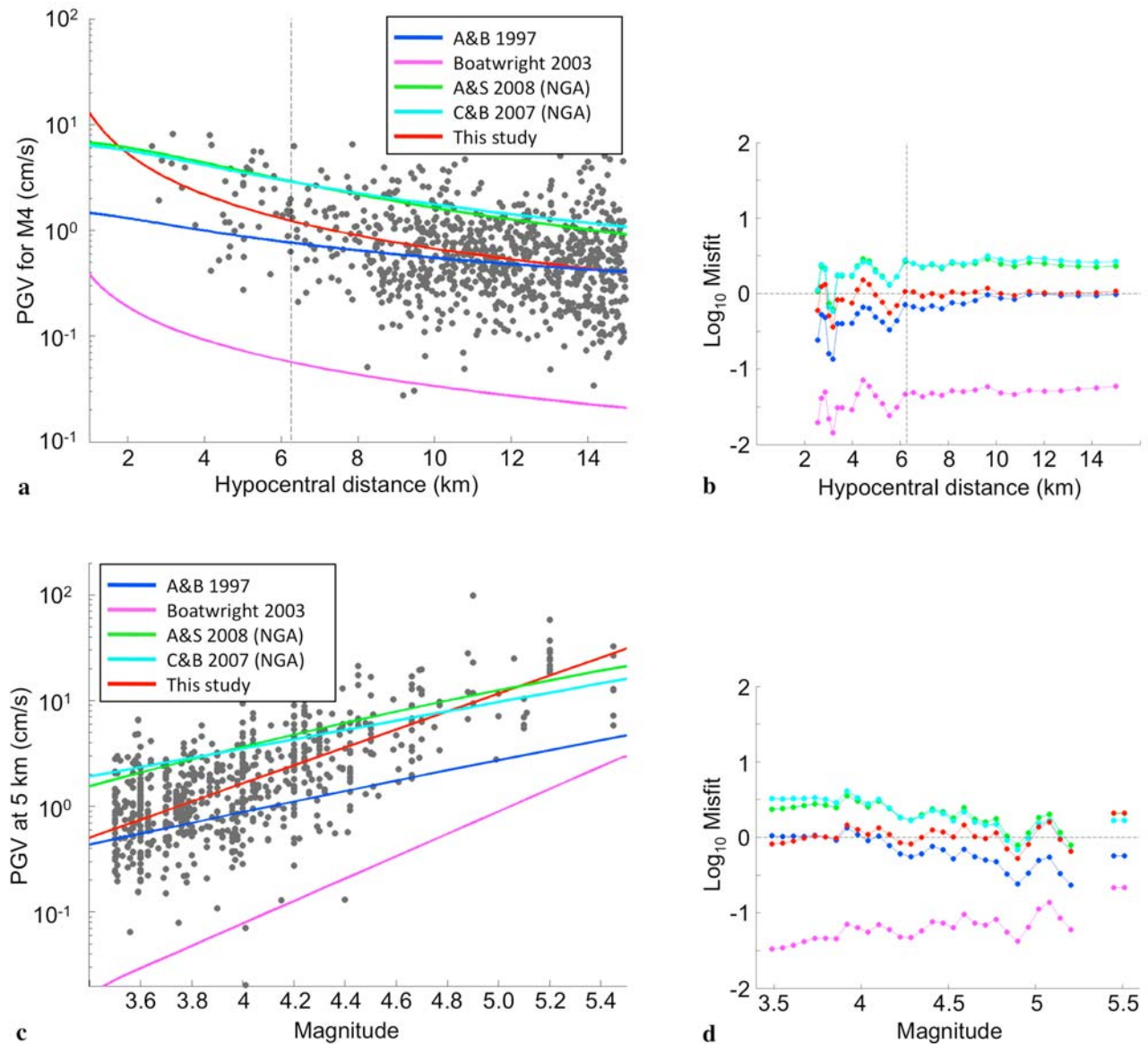
Figure B1. Peak ground velocity regression based on California Shakemap data. (a) PGV as a function of distance for a M4 reference earthquake, using several published regressions (blue [*Atkinson and Boore*, 1997], magenta [*Boatwright et al.*, 2003], green [*Abrahamson and Silva*, 2008], cyan [*Campbell and Bozorgnia*, 2007]), as well as the regression found in this study (red curve). Gray dots are individual PGV measurements, rescaled to the reference magnitude, using the regression from this study. The vertical dashed line at ~6.2 km marks the boundary of the near-field region defined in this study. (b) $\log_{10}$ misfit (the predicted PGV divided by the observed PGV) for each of the regressions in Figure B1a as a function of distance. Misfits are averaged over magnitudes 3.5–5.5. Vertical dashed line as in Figure B1a. (c) PGV as a function of magnitude at a reference distance of 5 km. (d) $\log_{10}$ misfit as a function of magnitude for the various regressions, averaged over distances from 0 to 15 km.

with the constraint that constants c_2, c_3, and c_4 be positive. To make the regression as representative of near-field measurements as possible, the data are weighted by the space between data points. This is roughly equivalent to fitting the regression curve to binned data. The best fit regression parameters are given in Table 1 (first row). The 95% confidence levels for each parameter are computed from 1000 bootstrap resamplings of the Shakemap data. The regression always finds $c_4 = 0$ km, and therefore, we do not report error bounds on this parameter. However, due to the lack of data at very

small distances, we must consider this parameter somewhat ill-constrained. The regression and regression misfit are plotted against distance and magnitude in Figure B1, along with several other published regressions for comparison. This regression is the most appropriate proxy for dynamic strain in our magnitude and distance range, as it is conditioned entirely on data within this range.

[87] For use in the ETAS simulation, we also perform a regression in which the magnitude scaling constant c_2 is constrained to equal 1 (Table 1, second row). This is for con-

sistency with known aftershock scaling with magnitude. This constraint does not significantly alter the spatial component of the regression.

Appendix C: Calculation of Earthquake Probability From $\overline{R}$

[88] Appendix A shows how to transform the distribution of R into fractional earthquake rate change n, assuming Poisson distributed interevent times. The same statistical model can be used to calculate the probability of triggering an earthquake given the estimated rate change. For a homogeneous Poisson process, the probability of observing exactly m events in time period t, given the average event rate λ, is given by

$$P\left(N_{EQ} = m | \lambda t\right) = \frac{(\lambda t)^m e^{-\lambda t}}{m!}. \tag{C1}$$

The probability of observing one or more events is equal to 1 minus the probability of observing zero events,

$$P\left(N_{EQ} > 0 | \lambda t\right) = 1 - P\left(N_{EQ} = 0 | \lambda t\right) = 1 - \exp\{-\lambda t\}. \tag{C2}$$

Over one recurrence interval (time $t = \lambda_1^{-1}$), the probability of observing at least one event given fractional rate change n is

$$P\left(N_{EQ} \geq 1 | n\right) = 1 - \exp\{-(n+1)\}. \tag{C3}$$

That is, if the average seismicity rate was one earthquake per day, the probability of seeing an earthquake on any given day, in the absence of triggering, is about 63%. Equation (C3) then gives the adjusted probability of seeing that "daily" earthquake given the increase in seismicity rate measured by n. Equation (C3) is equation (8) in the main text.

Appendix D: Modified ETAS Simulation

[89] The epidemic-type aftershock sequence (ETAS) model uses empirical probability distributions to stochastically generate realistically clustered earthquake catalogs [Ogata, 1998]. We briefly summarize the governing equations here and direct the interested reader to the studies cited in the main text for more information.

[90] 1. Earthquake magnitudes are assigned from a Gutenberg-Richter probability distribution,

$$N(M) = 10^{a-bM}, \tag{D1}$$

where N is the number of earthquakes with magnitude greater than or equal to M, and a and b are constants, with b typically around 1.

[91] 2. The temporal decay of aftershock sequences is governed by the modified Omori's law, which states that aftershock rate decreases approximately as 1 over the time since the main shock,

$$R(t) \propto (c+t)^{-p}, \tag{D2}$$

where R is the instantaneous aftershock rate, c is a constant that effectively keeps the rate finite at zero time, and p is the decay exponent.

[92] 3. An aftershock productivity law is necessary to close the equations in time and magnitude. Previous work shows that the number of aftershocks scale exponentially with main shock magnitude [Felzer et al., 2004; Helmstetter et al., 2005].

$$N_{AS} \propto 10^{\alpha M}, \tag{D3}$$

where α is a constant near 1 and M is main shock magnitude. Equations (D2) and (D3) are related, in that the integral of $R(t)$ over the duration of the aftershock sequence equals N_{AS}, and we define a productivity constant A, such that

$$N_{AS} = \int_0^\infty \frac{A \times 10^{\alpha(M-M_{min})}}{(c+t)^p} dt, \tag{D4}$$

where M_{min} is the minimum magnitude in the simulation. For $p > 1$, N_{AS} is finite. For $p \leq 1$, N_{AS} must be calculated over a finite time period. Equation (D4) is calibrated to reproduce Båth's law (with $\alpha = 1$), which states that the largest aftershock of a sequence is on average ~1 magnitude unit below the main shock magnitude.

[93] 4. A full space-time simulation also requires a law describing the spatial clustering of aftershocks. For example, Felzer and Brodsky [2006] give

$$\rho(r) \propto r^{-\gamma}, \tag{D5}$$

where ρ is linear aftershock density at distance r from the main shock and γ is a constant.
We replace rules (3) and (4) with an equivalent rule that also reproduces Båth's law and a power law decrease in linear aftershock density but is based on dynamic strain rather than magnitude. The equivalent rule specifies that the number of aftershocks per unit area scales linearly with peak dynamic strain,

$$N_{AS} = \kappa \varepsilon_{dyn}. \tag{D6}$$

Accordingly, we set $\gamma = c_3$ from the constrained PGV regression (Table 1, second row).
[94] The constant of proportionality κ is found by dividing the number of aftershocks predicted by equation (D4) by the peak dynamic strain integrated over the aftershock zone (equation (7)). This gives

$$\kappa = \frac{C_S A \times 10^{-c_1-M_{min}} c^{1-p}(1-\gamma)}{2\pi(p-1)\left(D_{max}^{1-\gamma} - D_{min}^{1-\gamma}\right)}, \tag{D7}$$

where C_S is the shear wave speed, c_1 is the first PGV regression parameter (Table 1, second row), A, c, and p are the ETAS constants, and D_{max} and D_{min} are the maximum and minimum bounds of the local aftershock zone, imposed to make the simulation numerically tractable. For the ETAS simulation, we refit the PGV regression constraining $c_2 = 1$, consistent with $\alpha = 1$ in equation (D3). The fit parameters for the constrained regression are reported in Table 1 (second row).
[95] Remotely triggered earthquakes are generated in proportion to κ times their dynamic strain amplitude. In this way, triggering associated with both local earthquakes and

the surface waves of distant earthquakes is simulated simultaneously in a self-consistent manner.

[96] We use a version of Felzer and Felzer's Matlab code, modified to include a separate catalog of global triggers (http://pasadena.wr.usgs.gov/office/kfelzer/AftSimulator. html) [*Felzer et al.*, 2002]. This code was also used by *Hardebeck et al.* [2008]. An estimate of the spatially varying California background seismicity rate is included with the code (Figure 13b), as well as estimates of ETAS parameters representative of California (Table 2). The dimensions of the aftershock zone, specified for computational efficiency and to keep the number of aftershocks finite, are left at the default values of $D_{min} = 0.001$ km and $D_{max} = 500$ km, respectively.

References

Abrahamson, N., and W. Silva (2008), Summary of the Abrahamson and Silva NGA ground-motion relations, *Earthquake Spectra*, 24, 67–97.

Aki, K., and P. G. Richards (2002), *Quantitative Seismology*, 2nd ed., 700 pp., Univ. Sci. Books, Sausalito, Calif.

Anderson, J. G., J. N. Brune, J. N. Louie, Y. H. Zeng, M. Savage, G. Yu, Q. B. Chen, and D. Depolo (1994), Seismicity in the western Great Basin apparently triggered by the Landers, California, earthquake, 28 June 1992, *Bull. Seismol. Soc. Am.*, 84(3), 863–891.

Atkinson, G. M., and D. M. Boore (1997), Some comparisons between recent ground motion relations, *Seismol. Res. Lett.*, 68(1), 24–40.

Beeler, N. M., and D. A. Lockner (2003), Why earthquakes correlate weakly with the solid Earth tides: Effects of periodic stress on the rate and probability of earthquake occurrence, *J. Geophys. Res.*, 108(B8), 2391, doi:10.1029/2001JB001518.

Boatwright, J., K. Thywissen, and L. C. Seekins (2001), Correlation of ground motion and intensity for the 17 January 1994 Northridge, California, earthquake, *Bull. Seismol. Soc. Am.*, 91(4), 739–752.

Boatwright, J., H. Bundock, J. Luetgert, L. Seekins, L. Gee, and P. Lombard (2003), The dependence of PGA and PGV on distance and magnitude inferred from northern California ShakeMap data, *Bull. Seismol. Soc. Am.*, 93(5), 2043–2055.

Brodsky, E. E. (2006), Long-range triggered earthquakes that continue after the wave train passes, *Geophys. Res. Lett.*, 33, L15313, doi:10.1029/2006GL026605.

Brodsky, E. E., and S. G. Prejean (2005), New constraints on mechanisms of remotely triggered seismicity at Long Valley Caldera, *J. Geophys. Res.*, 110, B04302, doi:10.1029/2004JB003211.

Brodsky, E. E., V. Karakostas, and H. Kanamori (2000), A new observation of dynamically triggered regional seismicity: Earthquakes in Greece following the August, 1999 Izmit, Turkey earthquake, *Geophys. Res. Lett.*, 27(17), 2741–2744.

Brodsky, E. E., E. Roeloffs, D. Woodcock, I. Gall, and M. Manga (2003), A mechanism for sustained groundwater pressure changes induced by distant earthquakes, *J. Geophys. Res.*, 108(B8), 2390, doi:10.1029/2002JB002321.

Campbell, K. W., and Y. Bozorgnia (2007), Campbell-Bozorgnia NGA ground motion relations for the geometric mean horizontal component of peak and spectral ground motion parameters, *Rep. 2007/02*, Pac. Earthquake Eng. Res. Cent., Berkeley, Calif.

Casella, G., and R. L. Berger (2002), *Statistical Inference*, 2nd ed., 660 pp., Thomson Learning, Pacific Grove, Calif.

Cochran, E. S., J. E. Vidale, and S. Tanaka (2004), Earth tides can trigger shallow thrust fault earthquakes, *Science*, 306, 1164–1166.

Dieterich, J. (1994), A constitutive law for rate of earthquake production and its application to earthquake clustering, *J. Geophys. Res.*, 99(B2), 2601–2618.

Elkhoury, J. E., E. E. Brodsky, and D. C. Agnew (2006), Seismic waves increase permeability, *Nature*, 441, 1135–1138.

Felzer, K. R., and E. E. Brodsky (2005), Testing the stress shadow hypothesis, *J. Geophys. Res.*, 110, B05S09, doi:10.1029/2004JB003277.

Felzer, K. R., and E. E. Brodsky (2006), Decay of aftershock density with distance indicates triggering by dynamic stress, *Nature*, 441, 735–738.

Felzer, K. R., T. W. Becker, R. E. Abercrombie, G. Ekstrom, and J. R. Rice (2002), Triggering of the 1999 M_W 7.1 Hector Mine earthquake by aftershocks of the 1992 M_W 7.3 Landers earthquake, *J. Geophys. Res.*, 107(B9), 2190, doi:10.1029/2001JB000911.

Felzer, K. R., R. E. Abercrombie, and G. Ekstrom (2004), A common origin for aftershocks, foreshocks, and multiplets, *Bull. Seismol. Soc. Am.*, 94, 88–98.

Freed, A. M. (2005), Earthquake triggering by static, dynamic, and postseismic stress transfer, *Annu. Rev. Earth Planet. Sci.*, 33, 335–367.

Freed, A. M., and J. Lin (1998), Time-dependent changes in failure stress following thrust earthquakes, *J. Geophys. Res.*, 103(B10), 24,393–24,409.

Gardner, J. K., and L. Knopoff (1974), Is the sequence of earthquakes in southern California, with aftershocks removed, Poissonian?, *Bull. Seismol. Soc. Am.*, 64(15), 1363–1367.

Gasperini, P., and B. Lolli (2006), Correlation between the parameters of the aftershock rate equation: Implications for the forecasting of future sequences, *Phys. Earth Planet. Inter.*, 156, 41–58.

Gomberg, J. (2001), The failure of earthquake failure models, *J. Geophys. Res.*, 106(B8), 16,253–16,263.

Gomberg, J., and D. Agnew (1996), The accuracy of seismic estimates of dynamic strains: An evaluation using strainmeter and seismometer data from Pinon Flat Observatory, California, *Bull. Seismol. Soc. Am.*, 86(1), 212–220.

Gomberg, J., and S. Davis (1996), Stress strain changes and triggered seismicity at the Geysers, California, *J. Geophys. Res.*, 101(B1), 733–749.

Gomberg, J., and K. Felzer (2008), A model of earthquake triggering probabilities and application to dynamic deformations constrained by ground motion observations, *J. Geophys. Res.*, 113, B10317, doi:10.1029/2007JB005184.

Gomberg, J., and P. Johnson (2005), Seismology: Dynamic triggering of earthquakes, *Nature*, 437, 830–830.

Gomberg, J., M. L. Blanpied, and N. M. Beeler (1997), Transient triggering of near and distant earthquakes, *Bull. Seismol. Soc. Am.*, 87(2), 294–309.

Gomberg, J., P. A. Reasenberg, P. Bodin, and R. A. Harris (2001), Earthquake triggering by seismic waves following the Landers and Hector Mine earthquakes, *Nature*, 411(6836), 462–466.

Gomberg, J., P. Bodin, and P. A. Reasenberg (2003), Observing earthquakes triggered in the near field by dynamic deformations, *Bull. Seismol. Soc. Am.*, 93(1), 118–138.

Gomberg, J., P. Bodin, K. Larson, and H. Dragert (2004), Earthquake nucleation by transient deformations caused by the $M = 7.9$ Denali, Alaska, earthquake, *Nature*, 427, 621–624.

Hainzl, S., F. Scherbaum, and C. Beauval (2006), Estimating background activity based on interevent-time distribution, *Bull. Seismol. Soc. Am.*, 96, 313–320.

Hardebeck, J. L., K. R. Felzer, and A. J. Michael (2008), Improved tests reveal that the accelerating moment release hypothesis is statistically insignificant, *J. Geophys. Res.*, 113, B08310, doi:10.1029/2007JB005410.

Harrington, R. M., and E. E. Brodsky (2006), The absence of remotely triggered seismicity in Japan, *Bull. Seismol. Soc. Am.*, 96, 871–878.

Helmstetter, A., and D. Sornette (2003), Predictability in the epidemic-type aftershock sequence model of interacting triggered seismicity, *J. Geophys. Res.*, 108(B10), 2482, doi:10.1029/2003JB002485.

Helmstetter, A., Y. Y. Kagan, and D. D. Jackson (2005), Importance of small earthquakes for stress transfers and earthquake triggering, *J. Geophys. Res.*, 110, B05S08, doi:10.1029/2004JB003286.

Hill, D. P. (2008), Dynamic stresses, Coulomb failure, and remote triggering, *Bull. Seismol. Soc. Am.*, 98, 66–92.

Hill, D. P., and S. G. Prejean (2007), Dynamic triggering, in *Treatise on Geophysics*, vol. 4, edited by H. Kanamori, pp. 257–292, Elsevier, New York.

Hill, D. P., et al. (1993), Seismicity remotely triggered by the magnitude 7.3 Landers, California, earthquake, *Science*, 260(5114), 1617–1623.

Holliday, J. R., D. L. Turcotte, and J. B. Rundle (2008), A review of earthquake statistics: Fault and seismicity-based models, ETAS and BASS, *Pure Appl. Geophys.*, 165, 1003–1024.

Hough, S. E. (2005), Remotely triggered earthquakes following moderate main shocks (or, why California is not falling into the ocean), *Seismol. Res. Lett.*, 76, 58–66.

Johnson, P. A., and X. Jia (2005), Nonlinear dynamics, granular media and dynamic earthquake triggering, *Nature*, 437, 871–874.

Joyner, W. B., and D. M. Boore (1981), Peak horizontal acceleration and velocity from strong-motion records including records from the 1979 Imperial Valley, California, earthquake, *Bull. Seismol. Soc. Am.*, 71(6), 2011–2038.

Kagan, Y. Y. (2004), Short-term properties of earthquake catalogs and models of earthquake source, *Bull. Seismol. Soc. Am.*, 94, 1207–1228.

Kagan, Y. Y., and D. D. Jackson (2000), Probabilistic forecasting of earthquakes, *Geophys. J. Int.*, 143(2), 438–453.

Kilb, D., J. Gomberg, and P. Bodin (2000), Triggering of earthquake aftershocks by dynamic stresses, *Nature*, 408(6812), 570–574.

King, G. C. P., R. S. Stein, and J. Lin (1994), Static stress changes and the triggering of earthquakes, *Bull. Seismol. Soc. Am.*, 84(3), 935–953.

Lay, T., and T. C. Wallace (1995), *Modern Global Seismology*, Academic, San Diego, Calif.

Love, A. E. H. (1927), *Mathematical Theory of Elasticity*, Cambridge Univ., Cambridge, U. K.

Marsan, D. (2003), Triggering of seismicity at short timescales following Californian earthquakes, *J. Geophys. Res.*, *108*(B5), 2266, doi:10.1029/2002JB001946.

Matthews, M. V., and P. A. Reasenberg (1988), Statistical methods for investigating quiescence and other temporal seismicity patterns, *Pure Appl. Geophys.*, *126*(2–4), 357–372.

Molchan, G. (2005), Interevent time distribution in seismicity: A theoretical approach, *Pure Appl. Geophys.*, *163*, 1135–1150.

Ogata, Y. (1992), Detection of precursory relative quiescence before great earthquakes through a statistical model, *J. Geophys. Res.*, *97*(B13), 19,845–19,871.

Ogata, Y. (1998), Space-time point-process models for earthquake occurrences, *Ann. Inst. Stat. Math.*, *50*(2), 379–402.

Ogata, Y. (1999), Seismicity analysis through point-process modeling: A review, *Pure Appl. Geophys.*, *155*(2–4), 471–507.

Parsons, T. (2005), A hypothesis for delayed dynamic earthquake triggering, *Geophys. Res. Lett.*, *32*, L04302, doi:10.1029/2004GL021811.

Peng, Z., J. E. Vidale, M. Ishii, and A. Helmstetter (2007), Seismicity rate immediately before and after main shock rupture from high-frequency waveforms in Japan, *J. Geophys. Res.*, *112*, B03306, doi:10.1029/2006JB004386.

Peng, Z. G., and P. Zhao (2009), Migration of early aftershocks following the 2004 Parkfield earthquake, *Nat. Geosci.*, *2*, 877–881.

Perfettini, H., and J. P. Avouac (2007), Modeling afterslip and aftershocks following the 1992 Landers earthquake, *J. Geophys. Res.*, *112*, B07409, doi:10.1029/2006JB004399.

Pollitz, F. F., and M. J. S. Johnston (2006), Direct test of static stress versus dynamic stress triggering of aftershocks, *Geophys. Res. Lett.*, *33*, L15318, doi:10.1029/2006GL026764.

Pollitz, F. F., R. Burgmann, and B. Romanowicz (1998), Viscosity of oceanic asthenosphere inferred from remote triggering of earthquakes, *Science*, *280*(5367), 1245–1249.

Prejean, S. G., D. P. Hill, E. E. Brodsky, S. E. Hough, M. J. S. Johnston, S. D. Malone, D. H. Oppenheimer, A. M. Pitt, and K. B. Richards-Dinger (2004), Remotely triggered seismicity on the United States West Coast following the M_W 7.9 Denali fault earthquake, *Bull. Seismol. Soc. Am.*, *94*, S348–S359.

Reasenberg, P. A., and L. M. Jones (1989), Earthquake hazard after a mainshock in California, *Science*, *243*(4895), 1173–1176.

Rezapour, M., and R. G. Pearce (1998), Bias in surface-wave magnitude M_s due to inadequate distance corrections, *Bull. Seismol. Soc. Am.*, *88*(1), 43–61.

Richter, C. F. (1935), An instrumental earthquake magnitude scale, *Bull. Seismol. Soc. Am.*, *25*(1), 1–32.

Saichev, A., and D. Sornette (2006), "Universal" distribution of inter-earthquake times explained, *Phys. Rev. Lett.*, *97*, 078501, doi:10.1103/Physrevlett.1197.078501.

Savage, H. M., and C. Marone (2008), Potential for earthquake triggering from transient deformations, *J. Geophys. Res.*, *113*, B05302, doi:10.1029/2007JB005277.

Scholz, C. H. (2003), Earthquakes—Good tidings, *Nature*, *425*(6959), 670–671.

Sornette, D., and M. J. Werner (2005a), Apparent clustering and apparent background earthquakes biased by undetected seismicity, *J. Geophys. Res.*, *110*, B09303, doi:10.1029/2005JB003621.

Sornette, D., and M. J. Werner (2005b), Constraints on the size of the smallest triggering earthquake from the epidemic-type aftershock sequence model, Bath's law, and observed aftershock sequences, *J. Geophys. Res.*, *110*, B08304, doi:10.1029/2004JB003535.

Spudich, P., L. K. Steck, M. Hellweg, J. B. Fletcher, and L. M. Baker (1995), Transient stresses at Parkfield, California, produced by the *M* 7.4 Landers earthquake of June 28, 1992: Observations from the UPSAR dense seismograph array, *J. Geophys. Res.*, *100*(B1), 675–690.

Stark, M. A., and S. D. Davis (1996), Remotely triggered microearthquakes at the Geysers geothermal field, California, *Geophys. Res. Lett.*, *23*(9), 945–948.

Stein, R. S., G. C. P. King, and J. Lin (1994), Stress triggering of the 1994 *M* = 6.7 Northridge, California, earthquake by its predecessors, *Science*, *265*(5177), 1432–1435.

Taira, T., P. G. Silver, F. L. Niu, and R. M. Nadeau (2009), Remote triggering of fault-strength changes on the San Andreas fault at Parkfield, *Nature*, *461*, 636–677.

Velasco, A. A., S. Hernandez, T. Parsons, and K. Pankow (2008), Global ubiquity of dynamic earthquake triggering, *Nat. Geosci.*, *1*, 375–379.

Wald, D. J., V. Quitoriano, T. H. Heaton, H. Kanamori, C. W. Scrivner, and C. B. Worden (1999), TriNet "ShakeMaps": Rapid generation of peak ground motion and intensity maps in California, *Earthquake Spectra*, *15*, 537–556.

Wald, D. J., B. C. Worden, V. Quitoriano, and K. L. Pankow (2006), ShakeMap manual: Technical manual, user's guide, and software guide, version 1.0, U.S. Geol. Surv., Reston, Va. (Available at http://pubs.usgs.gov/tm/2005/12A01/)

Walpole, R. E., and R. H. Myers (1989), *Probability and Statistics for Engineers and Scientists*, 4th ed., Macmillan, New York.

West, M., J. J. Sanchez, and S. R. McNutt (2005), Periodically triggered seismicity at Mount Wrangell, Alaska, after the Sumatra earthquake, *Science*, *308*, 1144–1146.

Wiemer, S. (2000), Introducing probabilistic aftershock hazard mapping, *Geophys. Res. Lett.*, *27*(20), 3405–3408.

Yamanaka, Y., and K. Shimazaki (1990), Scaling relationship between the number of aftershocks and the size of the main shock, *J. Phys. Earth*, *38*, 305–324.

Ziv, A. (2003), Foreshocks, aftershocks, and remote triggering in quasi-static fault models, *J. Geophys. Res.*, *108*(B10), 2498, doi:10.1029/2002JB002318.

E. E. Brodsky and N. J. van der Elst, Department of Earth and Planetary Science, University of California, 1156 High St., Santa Cruz, CA 95060, USA. (nvandere@ucsc.edu)